

DFT aided prediction of phase stability, optoelectronic and thermoelectric properties of A_2AuScX_6 (A= Cs, Rb; X= Cl, Br, I) double perovskites for energy harvesting technology

S. Mahmud^{1,2}, M.A. Ali¹, M. M. Hossain¹, M. M. Uddin¹

¹Advanced Computational Materials Research Laboratory, Department of Physics, Chittagong University of Engineering and Technology (CUET), Chattogram-4349, Bangladesh.

²Department of Electrical and Electronic Engineering, Jatiya Kabi Kazi Nazul Islam University (JKKNIU), Mymensingh-2224, Bangladesh.

Abstract

In this work, density functional theory (DFT) is used to find out the ground state structures of A_2AuScX_6 (A= Cs, Rb; X= Cl, Br, I) double Perovskite (DP) halides for the first time. The DP A_2AuScX_6 halides were studied for their structural phase stability and optoelectronic properties in order to identify potential materials for energy harvesting systems. The stability criteria were verified by computing the formation energy, binding energy, phonon dispersion curve, stiffness constants, tolerance, and octahedral factors. The electronic band structure, carrier effective mass, density of states (DOS), and charge density distribution were calculated to reveal the nature of electronic conductivity and chemical bonding nature present within them. For Cs_2AuScX_6 (Rb_2AuScX_6) [X = Cl, Br, I], the corresponding values of band gap [using TB-mBJ] are 1.88 (1.93), 1.68 (1.71), and 1.30 (1.32) eV. The optical constants (dielectric function, absorption coefficient, refractive index, energy loss function, photoconductivity, and reflectivity) were also calculated to get more insights into their electronic nature. For Cs_2AuScX_6 (Rb_2AuScX_6) [X = Cl, Br, I], the absorption coefficient in the visible range are 3.33 (3.45) $\times 10^5$ cm^{-1} , 2.70 (2.81) $\times 10^5$ cm^{-1} , and 2.13 (2.18) $\times 10^5$ cm^{-1} , respectively. We also investigated the thermoelectric properties to predict promising applications in thermoelectric devices. Our calculations revealed high ZT values of 0.92, 1.07, and 1.06 for Cs_2AuScX_6 (X = Cl, Br, I) and 0.97, 0.99, and 1.01 for Rb_2AuScX_6 (X = Cl, Br, I) at 300 K. To further aid in predicting any novel materials, routine research was also done on the thermo-mechanical characteristics. The results suggest the compounds considered as potential candidates for use in solar cells and/or thermoelectric devices.

Keywords: Double Perovskite halides; DFT computation; Phase stability; Optoelectronic properties; Thermo-electric properties; Thermo-mechanical properties.

1. Introduction

In the last few years, the energy demand has grown quickly, which has made experts work harder to find alternative sources of energy other than the use of fossil fuels along with additional usual sources. Sunlight, which is natural and provides a lot of energy, is a significant power system option¹. Researchers have paid tremendous attention to developing affordable and dependable materials that can significantly use solar radiation to produce energy. The photovoltaic process represents a viable means of generating renewable energy², and additional study is required to predict solar cell materials with superior efficiency.

The rapid increase in energy consumption over the past several years has pushed scientists to identify more conventional and alternative energy sources that do not need the burning of fossil fuels. Naturally occurring and abundant in energy, sunlight is a major power system option¹. Scientists have worked hard to predict reliable, inexpensive materials that can harness a considerable amount of solar radiation to generate electricity. The photovoltaic method is a feasible way to produce renewable energy², but further research is needed to identify solar cell materials with higher efficiency.

A semiconductor called Perovskite is employed to carry the electric charge whenever light strikes the substance. The chemical formula for the Perovskite crystal structure is ABX_3 , where A and B are cations, and X is an anion. A type of substance known as "double Perovskite" has a Perovskite crystal structure, but two distinct cations occupy the B-site of the structure. A double Perovskite has the formula $A_2BB'X_6$ because the B-site contains two distinct cations. The B and B' cations may alter, but the A-site cation stays the same as in a typical Perovskite. This configuration offers various features and capabilities and permits different cation combinations. The double Perovskite (DP) structure of A_2AuScX_6 ($A = Cs^+/Rb^+$; $X = Cl^-/Br^-/I^-$) consists of two interpenetrating face-centered cubic lattices, one formed by Cs^+/Rb^+ cations and the other by Au^{1+} , Sc^{3+} , and X^- anions. The choice of Au and Sc as the transition metal cations in each substance are particularly significant. Au is a noble metal known for its excellent electrical conductivity, while Sc is recognized for its tunable bandgap and favorable optoelectronic properties. Combining these two elements in the B-site of the double Perovskite halide makes it

possible to tailor the material's electronic band structure and charge transport properties. This tunability is essential for optimizing the material's performance in electronic and optoelectronic devices. The halide component, X (chloride, bromide, or iodide), plays a crucial role in determining the overall properties, especially influencing the electronic band structure and affecting the material's absorption characteristics. Also, by controlling the halide composition, researchers can modulate the energy levels and light absorption properties of materials, further enhancing their potential for optoelectronic applications. The main thing to remember is that DP can support B-site elements with oxidation states ranging from 1^+ to 4^+ , whereas ABX_3 can only handle 2^+ B-site cations³. Moreover, the zero oxidation state, a charge balance typical of Perovskite halides, may be recognized by combining tetravalent ions with a vacancy at BB'. Moreover, the band gap would be direct or indirect with larger values is impractical for solar cell use.

The organic-inorganic mixed or hybrid halide Perovskite $CH_3NH_3PbX_3$ ($MAPbX_3$; X= Cl/Br) has received a lot of interest as a key component in the fabrication of extremely effective solar cells due to its excellent efficiency⁴⁻⁹. Scientists have put in a lot of work to increase efficiency from 3.8% in 2009 to 26.08% in 2023¹⁰⁻¹⁴. The strong absorbance of light in the visible area and outstanding stability of organic-inorganic mixed or hybrid halide perovskite lead to their superior performance^{15,16}. However, lead (Pb), which cannot be commercialized on a big scale due to its poor stability and toxicity, necessitates the search for other materials as alternatives for B-sites.

Recently, there has been a lot of excitement in double perovskite (DP) halides due to their potential applications in various fields, including opto-electronics¹⁷⁻¹⁹, magnetism²⁰⁻²², catalysis²³⁻²⁵, and energy conversion^{5,26-28}. They also have a range of exciting properties that make them potential for next-generation electronic devices and energy technologies, including magneto-resistance²⁹, multi-ferroicity³⁰, and high spin-orbit coupling³¹. The DP halide group creates a new photovoltaic and optoelectronic device, but it is challenging to determine which ones have the optimum electrical, structural, and energetic properties for solar cell applications. Recently, DP has gained importance in optoelectronic studies^{32,33} because of its capacity to accept a variety of metal cations. Scientists are now studying DP to develop new materials with enhanced functionality and better understand the structure-property correlations associated with these materials. These materials might eventually lead to the development of more efficient and

eco-friendly devices, and they offer a great deal of promise to enhance technology across a range of sectors. For example, in the case, Slavney et al.³² prepared and examined $\text{Cs}_2\text{AgBiBr}_6$ double Perovskite and stated that inorganic compositions are interesting choices for optical and solar applications and should be explored extensively. McClure³⁴ experimentally synthesized the $\text{Cs}_2\text{AgBiX}_6$ (X= Cl/Br) solid solution and found the indirect band gap of 2.77 and 2.19 eV that are somewhat less than the band gaps of the similar lead halide Perovskites, 3.00 eV for $\text{CH}_3\text{NH}_3\text{PbCl}_3$ and 2.26 eV for $\text{CH}_3\text{NH}_3\text{PbBr}_3$. F. Igbari et al.³⁵ effectively prepared $\text{Cs}_2\text{AgBiBr}_6$ with an energy gap measured at 1.95 eV, suggesting as a potential photovoltaic material. A DP of $\text{Cs}_2\text{AgInCl}_6$ with a high photosensitive characteristics and a direct band nature was created by Volonakis et al.³⁶. In addition, many researchers have used the DFT approach for double halide Perovskite in solar cell, since it is a cost-effective and time-efficient alternative. Dhar et al. studied the lead free DP halide of $\text{Cs}_2\text{ScInX}_6$ (X= Cl/Br) compound theoretically and found the direct band gap of 0.637 and 0.81eV for optoelectronic device^{3,37}. N.E. et al. showed the optoelectronic and thermal properties of $\text{Cs}_2\text{ScTiX}_6$ (X= Cl/Br/I) for renewable energy applications with the band gap of 3.85 eV (direct), 3.2 (direct), and 2.75 eV (indirect). But these compounds exhibited better thermoelectric properties (figure of merit 0.61 to 0.66) compared to Cs based halide³⁸. Recently, Ashiq et al. developed B-site cations of Sc and Au based K_2ScAuZ_6 (Z= Br/I) DP halides for harvesting energy appliances with the indirect band gap values of 2.00 and 1.45 eV with ZT values of 0.80 and 1.00 at 200K³⁹.

We selected a group of double halide compounds of A_2AuScX_6 (A= Cs, Rb; X= Cl, Br, I). Six halides are present here: the alkaline metal Cs/Rb (group 1) and the rare earth soft metal Sc (group 3) are both paramagnetic, while the metal Au (group 11) is diamagnetic. To our knowledge, the aforementioned materials have not been the subject of any theoretical or applied research. Prediction of some new materials with better optoelectronic properties suitable for energy technologies is the primary goal of the present research.

Thus, the stability, optoelectronic characteristics, and thermoelectric properties of A_2AuScX_6 halides (where A = Cs, Rb, and X = Cl, Br, I) have been studied in this work. We anticipate that our study will offer vital guidance for predicting lead-free DP materials that may be used in future thermoelectric devices and/or solar cells. In addition, as a routine check, this article also discussed the thermo-mechanical characteristics of the named solids.

2. Computational technique

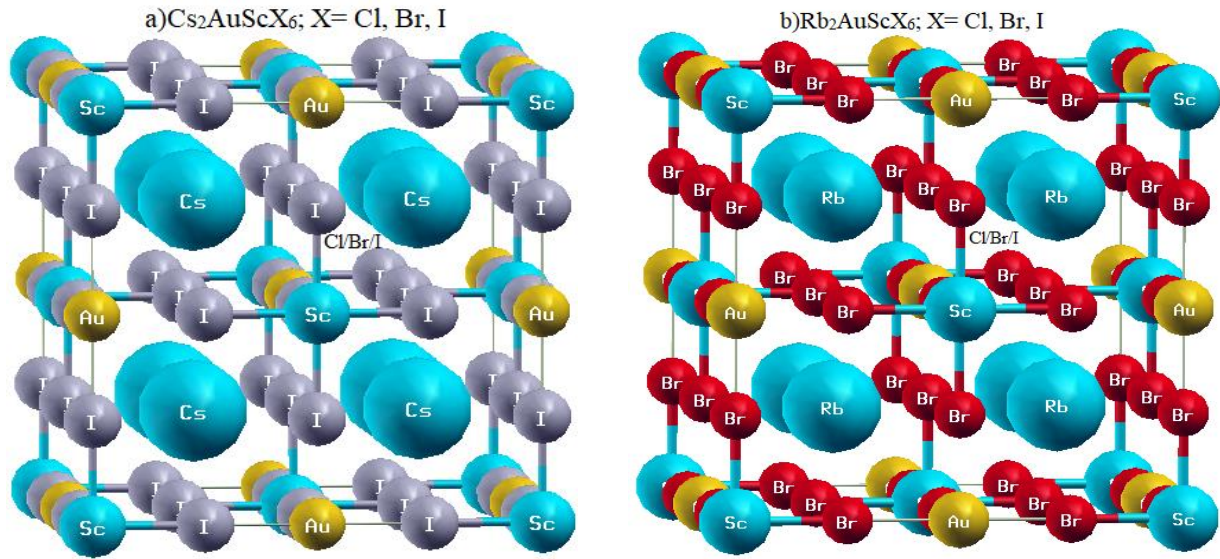
This task was carried out by the Wien2k code⁴⁰ using the DFT on the Kohn Shams equation. For this, firstly, ground state variables are computed using the Generalized Gradient Approximation (GGA) Perdew-Burke-Ernzerhof (PBE)⁴¹ approach with FP-LAPW (Full potential linearized augmented plane wave)⁴² method for structural optimization by establishing the Birch-Murnaghan 3rd state of equation. Initialization was performed using the following parameters: bond length factor of 3, the energy required for valence and core state separation of -6.0 Ry, R-MT*K-MAX of 7, number of employed k-points of 1000 (10×10×10), and GMAX of 12. The DFT calculation in Wien2k involves SCF (self-consistent field), which solves the Kohn Shams equation by updating the charge density on the electronic wave function. When calculating SCF, the energy convergence (ec) and charge convergence (cc) criteria are set at 0.0001Ry and 0.001e, respectively. Thermal and mechanical investigations are also conducted using the IR-Elast program⁴³. In order to deliver more accurate results, we used the Trans Blaha modified Becke-Johnson (TB-mBJ)⁴⁴ methodology for optoelectronic characteristics since it maintains a balance between precision and computing time for inorganic compounds. The Boltztrap2 algorithm⁴⁵ was used to determine the behavior of thermal electronic transport, with the exception of lattice vibration. The 1×1×1 supercell concept was used to perform the calculation of phonons using the technique of finite displacement way. For this computation, we used the following electron-valence configurations: 5p⁶6s¹ for the Cs, 4p⁶5s¹ for the Rb, 5d¹⁰6s¹ for the Au, 4s²3d¹ for the Sc, 3s²3p⁵ for the Cl, 4s²4p⁵ for the Br, and 5s²5p⁵ for the I.

3. Results and discussion

3.1 Structural properties and stability

Figure 1 depicts the cubic crystal structure of A₂AuScX₆ (A= Cs, Rb; X = Cl, Br, I) double perovskite (DP) halides, where the four formula units are present in the ratio of 2:1:1:6, and are comparable to the basic perovskite of ABX₃. The DP structures are made up of 8 Cs/Rb atoms, 13 [Au-X₆] octahedra and 14 [Sc-X₆] octahedra. These are all members of the face-centered Fm-3m (225) symmorphic space group and are located in the Wyckoff positions such as 8c, 4a, 4b, and 24e of the corresponding atoms Cs/Rb (0.25, 0.25, 0.25), Au (0.5, 0.5, 0.5), Sc (0, 0, 0), and Cl/Br/I (0.25, 0, 0). In this work, the lattice constant increases consistently as the halide atom transitions from Cl to Br to I. The crystal structure was optimized using the GGA-PBE (for

Wien2k) function. Table 1 displays the estimated lattice parameter with the lowest energy at the optimum volume



. Fig.1: Unit cell of a) $\text{Cs}_2\text{AuScX}_6$ and b) $\text{Rb}_2\text{AuScX}_6$; (X= Cl, Br, I)

The DP structural materials for cubic system's stability are determined by tolerance factor (t_G) and octahedral factor (μ) which was established by Goldsmith⁴⁶ and the following equations are given below:

$$t_G = \frac{R_A + R_X}{\sqrt{2}\left(\frac{R_{B'} + R_{B''}}{2} + R_X\right)}$$

$$\mu = \frac{R_{B'} + R_{B''}}{2R_X}$$

Where R represents the efficient ionic radii of each element in the above expressions. So that $R_A = 1.88$ and 1.72 for Cs^+ and Rb^+ , $R_{B'} = 1.37$ for Au^+ , $R_{B''} = 0.745$ for Sc^{3+} and $R_X = 1.81, 1.96, 2.2$ for $\text{Cl}^-, \text{Br}^-,$ and I^- which were taken by the Shannon ionic radius⁴⁷. Table 1 presents the obtained tolerance and octahedral factors of titled materials, and these results witness the stable structures within the range of 0.81 to 1.1 and 0.41 to 0.89⁴⁸, respectively.

Furthermore, the formation energy and binding energy serve as further confirmation for the dynamic stability of the DP halides of A_2AuScX_6 , which is calculated by the following equations⁴⁹:

$$E_f = \frac{E_{A_2AuScX_6} - n_A \times \frac{E_A}{k} - n_{Au} \times \frac{E_{Au}}{l} - n_{Sc} \times \frac{E_{Sc}}{m} - n_X \times \frac{E_X}{p}}{N}$$

$$E_b = E_{A_2AuScX_6} - n_A \times \mu_A - n_{Au} \times \mu_{Au} - n_{Sc} \times \mu_{Sc} - n_X \times \mu_X$$

Where, $E_{A_2AuScX_6}$ denotes the total energy of A_2AuScX_6 . E_A , E_{Au} , E_{Sc} , E_X and n_A , n_{Au} , n_{Sc} and n_X denotes the energy and number of atoms of Cs/Rb, Au, Sc, and Cl/Br/I, respectively. The coefficients k, l, m, p are the number of individual atoms per unit cell, and N is the total no of atoms in compounds. The μ represents the individual Free State energy of the total atom. The negative sign of formation energy confirmed their stability; higher negativity shows greater stability. Consequently, $A_2AuScCl_6$ is more stable than $A_2AuScBr_6$ and A_2AuScI_6 for the respective Cs and Rb-based halide.

To evaluate the mentioned compound's thermodynamic or chemical stability, we compute its decomposition energy by considering potential pathways. For this purpose, we use the experimentally identified stable phases of $CsAuCl_3$ ⁵⁰, $CsAuBr_3$ ⁵¹, $CsAuI_3$ ⁵², CsI ⁵³, RbI ⁵⁴, ScI_3 ⁵⁵, Au ⁵⁵ and proto-type of $Cs_3Cr_2Cl_9$ ⁵⁶ for Cl and Br based phase compound. The potential decomposition routes from OQMD for three halides based on Cs and Rb are as outlined below⁵⁵:

$$Cs_2AuScCl_6 = \frac{1}{4} CsAuCl_3 + \frac{7}{10} Cs_3Sc_2Cl_9 + \frac{1}{20} Au$$

$$Cs_2AuScBr_6 = \frac{1}{4} CsAuBr_3 + \frac{7}{10} Cs_3Sc_2Br_9 + \frac{1}{20} Au$$

$$Cs_2AuScI_6 = \frac{1}{4} CsAuI_3 + \frac{3}{10} CsI + \frac{2}{5} ScI_3 + \frac{1}{20} Au$$

$$Rb_2AuScCl_6 = \frac{1}{4} RbAuCl_3 + \frac{7}{10} Rb_3Sc_2Cl_9 + \frac{1}{20} Au$$

$$Rb_2AuScBr_6 = \frac{1}{4} RbAuBr_3 + \frac{7}{10} Rb_3Sc_2Br_9 + \frac{1}{20} Au$$

$$Rb_2AuScI_6 = \frac{1}{4} RbAuI_3 + \frac{3}{10} RbI + \frac{2}{5} ScI_3 + \frac{1}{20} Au$$

The decomposition enthalpies calculated for $Cs_2AuScCl_6$, $Cs_2AuScBr_6$, and Cs_2AuScI_6 are 23, 18, and 10 meV/atom, while for $Rb_2AuScCl_6$, $Rb_2AuScBr_6$ and Rb_2AuScI_6 , they are 19, 15, and 8 meV/atom, respectively. The positive decomposition enthalpy values demonstrate these

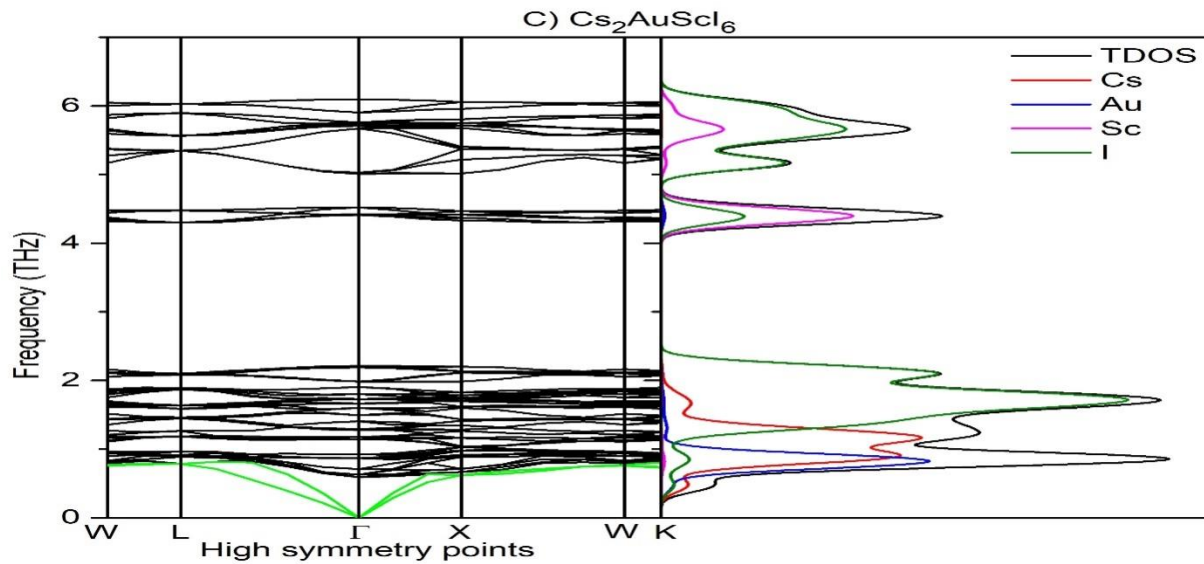
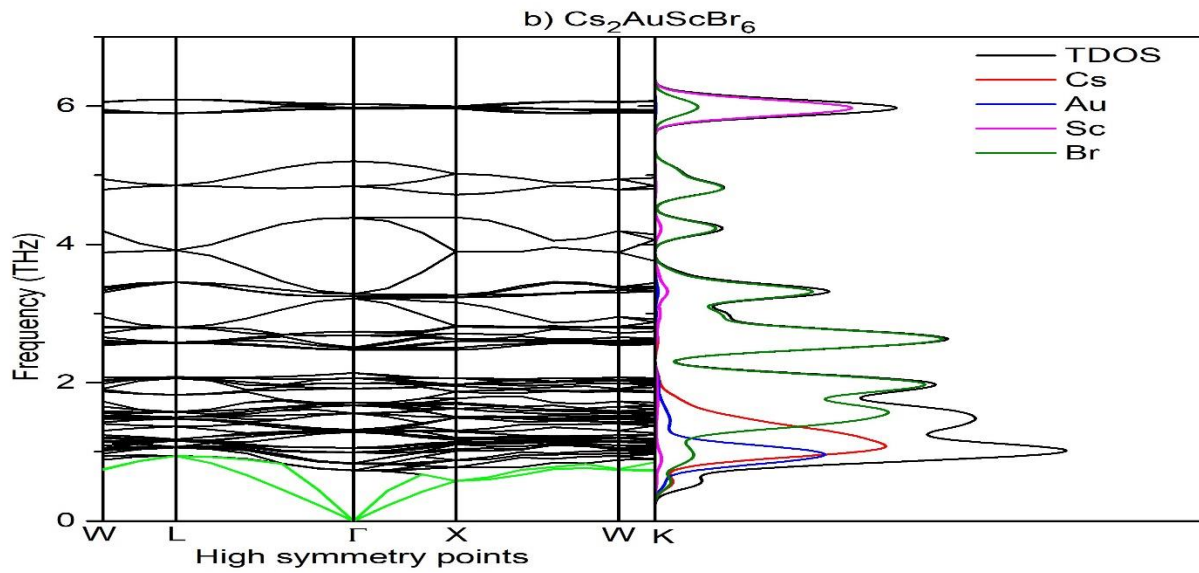
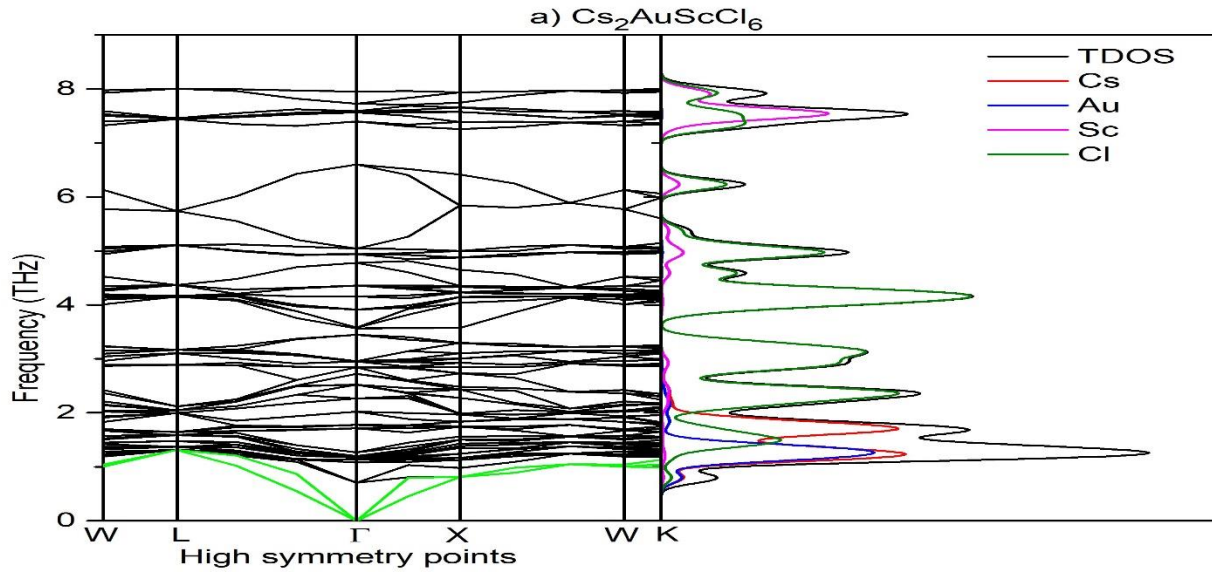
compound's thermodynamic stability, showing that the energy is derived from the compound's decomposing phases. The third-order Birch-Murnaghan equation of state⁵⁷, which supports cubic stability with non-magnetic characteristics and lowest energies, is used in the present samples to optimize the structural or energy volume of the named DPs. A solid's volume and the pressure it experiences are related by the Birch-Murnaghan 3rd-order equation of state, which is given below-

$$E(V) = E_0 + \frac{9V_0B_0}{16} + \left[\left\{ \left(\frac{V_0}{V} \right)^{2/3} - 1 \right\}^3 B'_0 + \left\{ \left(\frac{V_0}{V} \right)^{2/3} - 1 \right\}^2 - \left\{ 6 - 4 \left(\frac{V_0}{V} \right)^{2/3} \right\} \right]$$

Where $E(V)$ stands for the internal energy of the material, E_0 stands for minimum or ground state energy, V_0 stands for the reference or standard volume, V stands for the volume under stress, B_0 stands for zero pressure bulk modulus, and B'_0 stands for pressure modified bulk modulus. These substances have positive B'_0 values, indicating that they become stiffer when subjected to higher pressure. The ground state energy's negative value also represents the stability and growth of that stability for denser materials. The energy vs volume curve of the materials under investigation is shown by supplementary information (see Fig.1S). We have also determined the lattice constant (a) of all compounds from the E-V fitting curve. The atomic radius increases the lattice parameter in compositions based on Cl, Br, and I, and these shifts demonstrate the validity and accuracy of the study.

Table1: Optimized lattice parameter, volume, and structural entity with Fm-3m space group (#225) in non-polarized (NP) states of A_2AuScX_6 (A= Cs, Rb; X= Cl, Br, I).

| Parameter | $Cs_2AuScCl_6$ | $Cs_2AuScBr_6$ | Cs_2AuScI_6 | $Rb_2AuScCl_6$ | $Rb_2AuScBr_6$ | Rb_2AuScI_6 |
|------------------------|----------------|----------------|---------------|----------------|----------------|---------------|
| a=b=c (Å) | 10.5326 | 11.0869 | 11.8920 | 10.4480 | 11.0197 | 11.8452 |
| a=b=c(Bohr) | 19.9037 | 20.9513 | 22.4726 | 19.7438 | 20.8243 | 22.3841 |
| V (Bohr ³) | 1989 | 2290 | 2835 | 1924 | 2257 | 2788 |
| t_G | 0.90 | 0.89 | 0.87 | 0.87 | 0.86 | 0.85 |
| μ | 0.58 | 0.53 | 0.48 | 0.58 | 0.53 | 0.48 |
| E_F (eV/atom) | -2.38 | -2.00 | -1.56 | -2.34 | -1.95 | -1.50 |
| E_b (eV/atom) | -4.03 | -3.65 | -3.25 | -4.01 | -3.63 | -3.22 |
| E_0 (Ry) | -76324.63 | -102066.17 | -156214.92 | -57089.40 | -82830.94 | -136979.68 |
| B_0 | 34.38 | 32.38 | 23.20 | 34.87 | 30.75 | 24.52 |
| B'_0 | 6.03 | 5.52 | 4.42 | 5.39 | 4.40 | 3.74 |



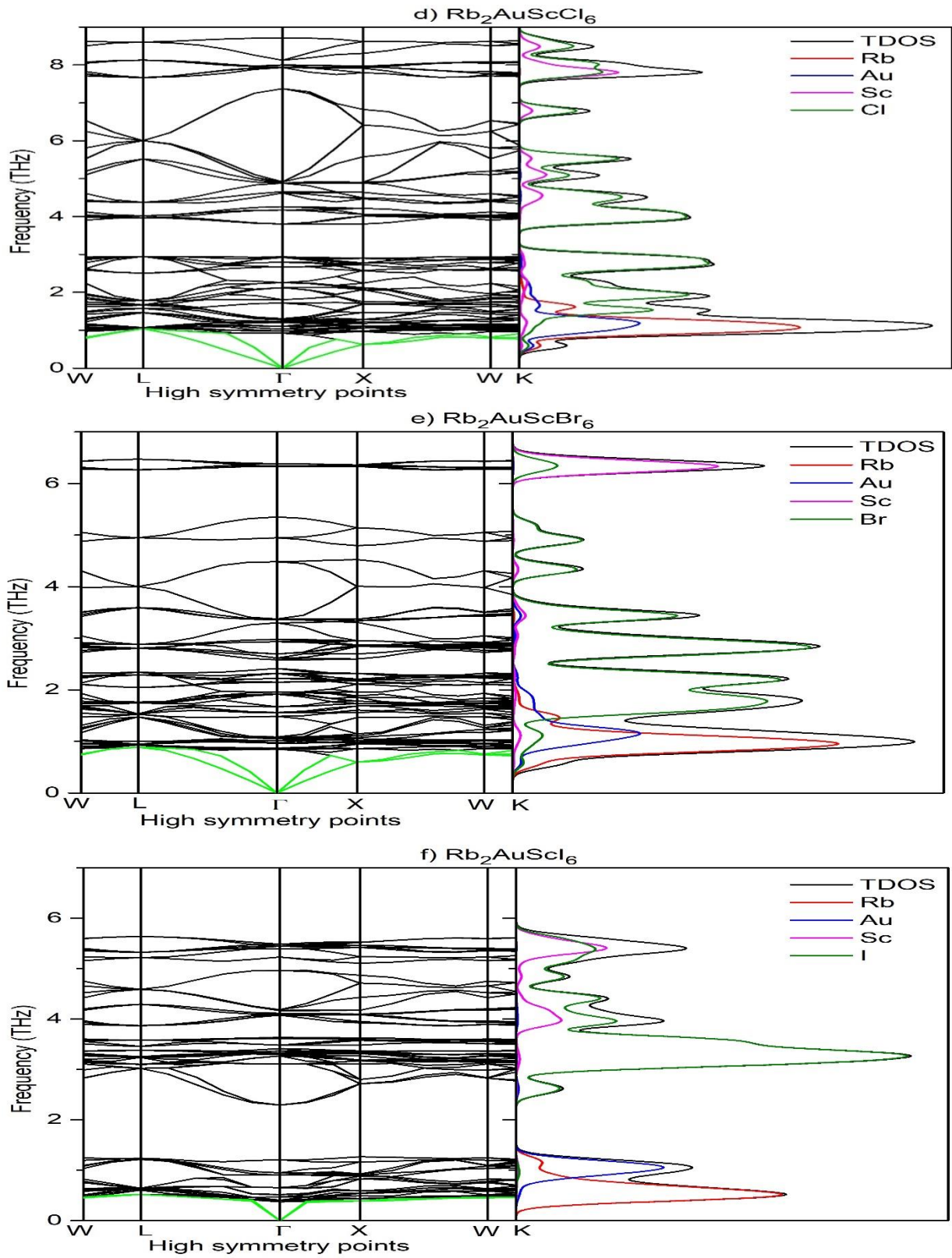


Fig.2: Phonon dispersion with DOS of a) $\text{Cs}_2\text{AuScCl}_6$, b) $\text{Cs}_2\text{AuScBr}_6$, c) $\text{Cs}_2\text{AuScI}_6$, d) $\text{Rb}_2\text{AuScCl}_6$, e) $\text{Rb}_2\text{AuScBr}_6$, f) $\text{Rb}_2\text{AuScI}_6$.

The phonon dispersion curve (PDC) of A_2AuScX_6 ($A = Cs, Rb$; $X = Cl, Br, I$) with PDOS is depicted in Fig. 2. The PDCs lack of negative frequencies in the band dispersion, where acoustic modes converge at gamma symmetry stations, supports the dynamical equilibrium. The dynamic stability of all drugs under investigation is demonstrated by the lack of an imagined mode during the whole BZ. With 10 atoms, these unit cell compositions must have $3N$, or 30 vibrational modes, of which three are acoustic and operate in the low-frequency region (less than 1 THz), and the remaining 27 are optic and operate in the high-frequency range (greater than 1 THz). These are known as zero point frequency and non-zero point frequency, respectively. All compound's phonon particles are stable along the following routes: W to L, L to Γ , Γ to X, X to W, and W to K. The compound's phonon DOS (PDOS) is displayed next to the dispersion curve for better understanding. We observed a strong peak in PDOS for flat bands and a negligible peak for non-flat bands. Both the phonon DOS and the frequency dispersion are precisely adjusted. It is shown that the low-frequency (below 2 THz) lattice vibrations coincide with the optic modes and are mainly ascribed to contributions from Cs and Au atoms.

In contrast, the halide ions (for Cl and Br) dominate the mid-level vibrations, whereas Sc ions work in tandem with Cl/Br ions to dominate the high-frequency area in Cs and Rb-based double Perovskite (DP) halides. However, for Cs_2AuScI_6 and Rb_2AuScI_6 , there is a phononic gap in the middle-frequency range, and I ions work in concert with Sc to generate high-frequency vibrations. As shown in the supplementary part (see Table S1), the poor lattice thermal conductivity of the investigated compounds was caused by the restriction of the phonon dispersion heat resulting from the overlap of acoustic and optical modes in the low-frequency ranges.

3.2. Electronic properties and the effective mass of charge carrier

The carrier transport channel may be seen visually through the features of conductors, semiconductors, and insulator's electronic characteristics. Further information about a material's intended applications may be gleaned from its electrical characteristics, such as its band structure and the distribution of electrons inside those bands (known as Total Density of States or Partial Density of States)⁵⁸. The A_2AuScX_6 ($A = Cs, Rb$; $X = Cl/Br/I$) material's band gap values are essential in deciding whether or not they may be used as photoelectric, optoelectronic, or any other type of particular purpose switching materials. We used the TB-mBJ potential⁵⁹ to forecast

the band gap with accuracy. Every material has an empty Fermi level, which indicates that it possesses a semiconducting nature. In addition, the materials are non-magnetic and show reductions (shifts) in the band structure at the Fermi level when Br or I replace Cl, the halide component.

The GGA-PBE functional technique was first used to investigate the electronic band structure. GGA-PBE + SOC was then employed to see whether there was any effect on the band arrangement. The band structure calculated using these functional methods revealed that the SOC impact on both compounds was very small (less than 0.04). The band structure of all materials under study is displayed in Figs. 3 and 4, utilizing the GGA-PBE (left side) and TB-mBJ (right side) approaches. Here, we present a comparative study of three methods for measuring the bandgap: the well-known TB-mBJ technique, the SCF with SOC, and the traditional SCF.

According to calculations made using the GGA-PBE (TB-mBJ) potential, the energy gaps for $\text{Cs}_2\text{AuScCl}_6$, $\text{Cs}_2\text{AuScBr}_6$, $\text{Cs}_2\text{AuScI}_6$, $\text{Rb}_2\text{AuScCl}_6$, $\text{Rb}_2\text{AuScBr}_6$, and $\text{Rb}_2\text{AuScI}_6$ are 1.65 (1.88), 1.43 (1.68), 0.95 (1.30), 1.69 (1.93), 1.44 (1.71), and 0.97 (1.32) eV, respectively. The fact that the band gap of such substances decreases as the number of atoms of the X element grows lends credence to the idea of the present pattern of oscillations in the energy band gap. The bandgap of the titled materials and a few other similar materials using TB-mBJ are compared in Table 2, which further supports the validity of the computed results for the materials under investigation. Every compound shows the same pattern, and TB-mBJ corrects the GGA-PBE's inaccuracy. The high symmetric points of W (0.50, 0.25, 0.75), L (0.5, 0.5, 0.5), Γ (0, 0, 0), X (0.5, 0, 0), W (0.50, 0.25, 0.75), and K (0.375, 0.375, 0.75) were the destinations of the Brillion zone route. The top of the VB route and the bottom of the CB is more parabolic in shape in the GGA-PBE and TB-mBJ approaches.

The typical energy ranges of perovskite bands are from 0.8 to 2.2eV⁶⁰, and materials for photoelectric conversion (PEC) will be able to use this energy extensively. For PEC, the DP of A_2AuScX_6 (A= Cs/Rb; X = Cl/Br/I) have suitable band gap values, which have great promise to be used as highly photo-sensitive materials in the not-too-distant future. From Fig. 3 and 4, it is clear that the maximum of valence band (MVB) point and minimum of the conduction band (MCB) point occurs at various symmetry points ($L \rightarrow X$ for all studied compound by TB-mBJ

approach; $L \rightarrow \Gamma$ only for $\text{Cs}_2\text{AuScI}_6$ and $\text{Rb}_2\text{AuScI}_6$ by GGA-PBE approach), indicating that all DP have indirect band gaps that are semiconducting.

Table 2: Computed band gaps for Cs-based halide of $\text{Cs}_2\text{AuScCl}_6$, $\text{Cs}_2\text{AuScBr}_6$, $\text{Cs}_2\text{AuScI}_6$, and Rb-based halide of $\text{Rb}_2\text{AuScCl}_6$, $\text{Rb}_2\text{AuScBr}_6$, and $\text{Rb}_2\text{AuScI}_6$.

| Compound | GGA-PBE | TB-mBJ | Nature | Reference |
|------------------------------|---------|--------|----------|---------------|
| $\text{Cs}_2\text{AuScCl}_6$ | 1.65 | 1.88 | Indirect | This |
| $\text{Cs}_2\text{AuScBr}_6$ | 1.43 | 1.68 | Indirect | This |
| $\text{Cs}_2\text{AuScI}_6$ | 0.95 | 1.30 | Indirect | This |
| $\text{Rb}_2\text{AuScCl}_6$ | 1.69 | 1.93 | Indirect | This |
| $\text{Rb}_2\text{AuScBr}_6$ | 1.44 | 1.71 | Indirect | This |
| $\text{Rb}_2\text{AuScI}_6$ | 0.97 | 1.32 | Indirect | This |
| $\text{K}_2\text{AuScBr}_6$ | - | 2.00 | Indirect | ³⁹ |
| K_2AuScI_6 | - | 1.45 | Indirect | ³⁹ |

The band gaps estimated from the electronic band structure are less than that obtained from the absorption spectrum for indirect band gap semiconductors⁶¹. Because the band gap values of A_2AuScX_6 ($X = \text{Cl/Br/I}$; $A = \text{Cs/Rb}$) lie within the visible region of the EM (electromagnetic) spectrum, they can be used in solar cell devices. A recent report revealed a significant aspect of the indirect band gap semiconductors for photocatalytic applications owing to the lower radiative recombination rate⁶². Additionally, flat bands inside the CB are observed, indicating the existence of the second phase and potentially explaining the emergence of superconductivity⁶². This suggests that DP is a viable alternative for advanced uses in ultra-powerful magnet technology. The bands still have a detectable range but get broader when Cl replaces the halide Br/I atom.

Solar cells commonly employ silicon (Si) and germanium (Ge) because of their availability, self-passivation, and indirect band gap. Both a photon and a phonon are needed for an indirect band gap semiconductor to go from the valence band (VB) to the conduction band (CB), causing changes in momentum and energy. Since the two variables are inversely related, an ideal characteristic of an efficient solar cell is that the minority carrier diffusion length is higher than the absorber depth of the material⁶³. Despite lower light absorption in indirect semiconductors,

they often have a longer recombination lifetime and a larger diffusion length, making them viable for efficient solar cells with a sufficiently thick absorbing layer.

So, indirect band gap semiconductors are mostly preferred in thin film solar cells due to their weaker light absorption, enabling a broader photon energy range, including lower-energy solar photons^{64–66}. Moreover, materials with an indirect band gap are more defect-tolerant and generate less heat, crucial for solar cell durability. In concentrator photovoltaic, this heat reduction is especially advantageous. Additionally, tandem solar cells combine multiple materials with different band gaps for increased efficiency and can leverage indirect band gap materials to optimize energy conversion across the solar spectrum^{32,67,68}.

The term "effective mass of charge carriers" describes the mass of electrons or holes in a double Perovskite halide. Their effective mass is essential in determining how charge carriers behave and react to outside stimuli like an electric field. The effective mass in DP can vary depending on the specific material and its composition. It is influenced by the material's band structure, which, in turn, depends on the types of halides and other elements present in the Perovskite structure.

We have calculated the effective mass of charge carriers (electrons or holes) of DP of A_2AuScX_6 at high symmetry points of VBM and CBM. The formula used to determine the effective mass and hole by using E-K dispersion of respective materials is as follows:

$$m^* = \frac{\hbar^2}{(d^2E/dK^2)}$$

Where, $\hbar = 1.05 \times 10^{-34}$ J/s. From the E-K dispersion curve, we get the values of d^2E/dK^2 by using E-K curve fitting of the respective parabolic curve at any symmetry points. The computed effective mass values are presented in Table 3. It is obvious that the predicted effective mass values are far lower than those reported by others⁶¹ for other DPs. The reduced effective mass is advantageous for transferring carriers, which is very beneficial for solar materials. Therefore, the DPs of A_2AuScX_6 are all highly perfect photovoltaic materials and have much promise for use in various solar applications.

Table 3: Estimated effective masses of holes (m_h^*) and electrons (m_e^*) at the lowest point of CB (L) and Highest point of VB (X or Γ) of respective materials of A_2AuScX_6 (A= Cs, Rb; X= Cl, Br, I).

| Compound | Approach | m_h^*/m_0 | m_e^*/m_0 | m_h/m_e |
|-------------------------------------|-----------------|-------------------------------|-------------------------------|-----------------------------|
| Cs ₂ AuScCl ₆ | GGA-PBE | 0.32, 0.62 ^a | 0.15, 0.47 ^a | 2.13 |
| | TB-mBJ | 0.33, 0.61 ^a | 0.18, 0.46 ^a | 1.83 |
| Cs ₂ AuScBr ₆ | GGA-PBE | 0.28 | 0.14 | 2.00 |
| | TB-mBJ | 0.28 | 0.15 | 1.86 |
| Cs ₂ AuScI ₆ | GGA-PBE | 0.25 | 0.063 | 3.96 |
| | TB-mBJ | 0.25 | 0.14 | 1.78 |
| Rb ₂ AuScCl ₆ | GGA-PBE | 0.31 | 0.15 | 2.06 |
| | TB-mBJ | 0.32 | 0.18 | 1.77 |
| Rb ₂ AuScBr ₆ | GGA-PBE | 0.27 | 0.13 | 2.07 |
| | TB-mBJ | 0.27 | 0.14 | 1.92 |
| Rb ₂ AuScI ₆ | GGA-PBE | 0.25 | 0.064 | 3.90 |
| | TB-mBJ | 0.25 | 0.13 | 1.92 |

^aReference⁶¹ for Cs₂AgAsCl₆

Figure 6 shows the titled compound's total and partial DOS and the key band structure characteristics found by the TB-mBJ potential. It offers exact information as well as the involvement of every component. It is clear that every DP compound has the same atomic state characteristics and ways of contribution. 0 eV was chosen as the Fermi level. Due to the little contribution of X-p orbitals, the Sc-d orbitals with hybridization (molecular orbital bonding) account for the majority of the MCB (minimum of conduction band) point of A_2AuScX_6 . In DOS, the energy value of the band structure and the near E_F of CB match exactly. Au-d orbitals contribute the most to the maximum of the valence band (MVB) point, whereas X-p orbitals contribute the least. The band structure of PDOS and TDOS ultimately reflects the difference in energy levels between them. Rather than adding much to the band structure, the Cs⁺/Rb⁺ cation close to E_F mostly donates charges to preserve structural stability.

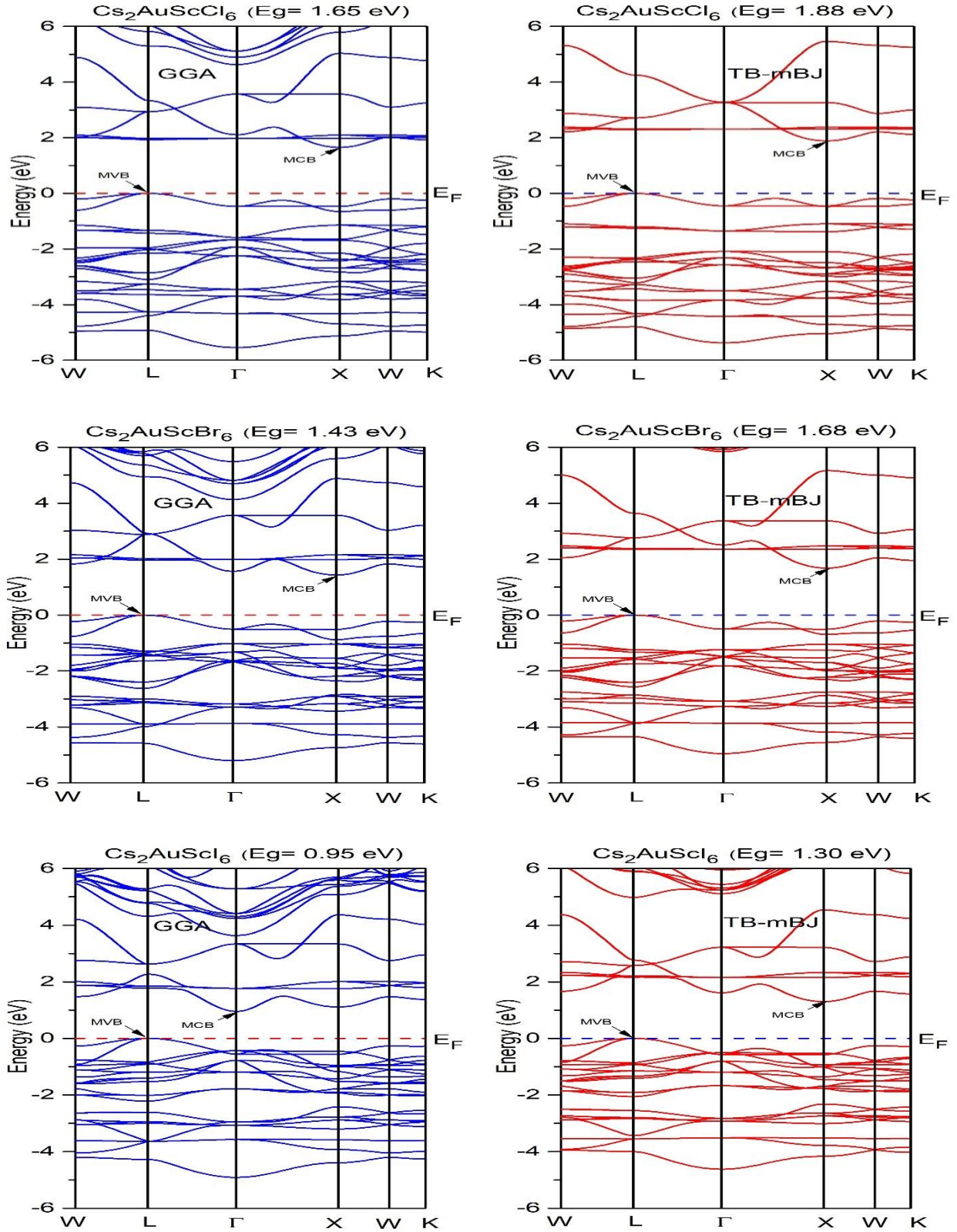


Fig.3: Energy band diagram of Cs-based halide of $\text{Cs}_2\text{AuScCl}_6$, $\text{Cs}_2\text{AuScBr}_6$, $\text{Cs}_2\text{AuScI}_6$ computed by GGA-PBE (Left side) and TB-mBJ (Right side) approach.

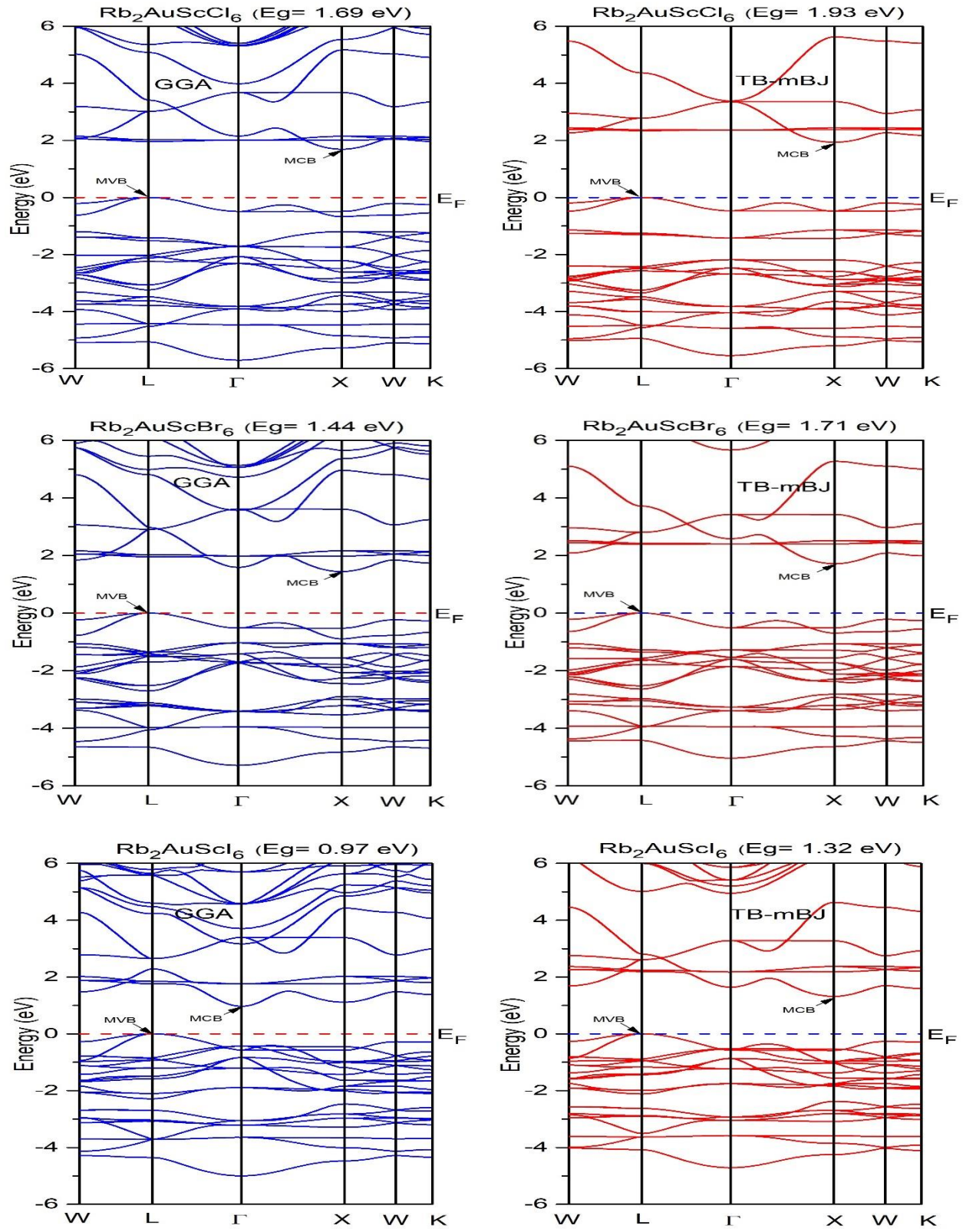


Fig.4: Energy band diagram of Rb-based halide of $\text{Rb}_2\text{AuScCl}_6$, $\text{Rb}_2\text{AuScBr}_6$, and $\text{Rb}_2\text{AuScI}_6$ computed by GGA-PBE (Left side) and TB-mBJ (Right side) method.

3.3. Nature of bonding

A_2AuScX_6 ($A = Cs/Rb$; $X = Cl/Br/I$) compounds belong to the DP family that have intriguing features because of their distinct bonding patterns and structure. It belongs to the class of inorganic DP, and the cations (Cs^+/Rb^+) and lattice have an impact on its characteristics. These material's charge density and bonding type can be examined regarding their crystal structure and internal electronic interactions. Space group $Fm-3m$ characterizes the cubic crystal structure of the chemical mentioned. The X ions (Cl, Br, or I) are positioned in the center of these octahedra in this structure, whereas the Au and Sc ions are situated in the corner, sharing octahedral positions. The spaces in between these octahedral Cs^+/Rb^+ ions are interstitial.

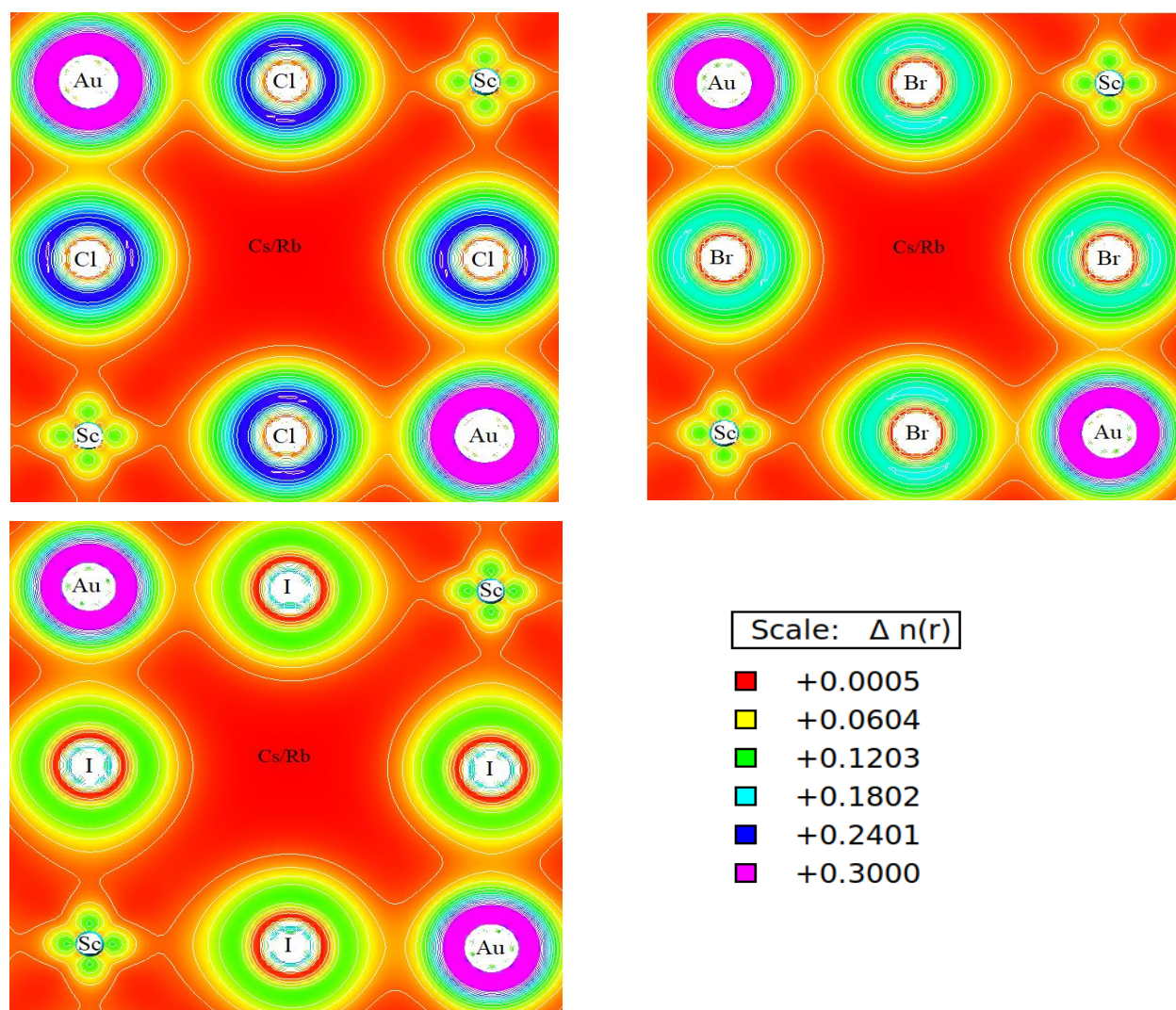


Fig.5: Contour plot of charge density of a) $A_2AuScCl_6$, b) $A_2AuScBr_6$, and c) A_2AuScI_6 ; [$A = Cs, Rb$].

This configuration creates a network of corner-sharing octahedra, which affects the compound's electronic and bonding characteristics. The charge density contour map for the materials in question is shown in Fig. 5.

The A ions (Cs/Rb) have relatively high electronegativity compared to Au and Sc, leading to ionic bonding between the A ions and the surrounding X ions. This results in forming A-X bonds with a certain degree of ionic character. The Au-Sc-X octahedral involves covalent bonding between the metal ions (Au and Sc) and the halogen ions (X). The electronegativity difference between the metal ions and X ions contributes to polar covalent bonds within the octahedral framework, similar to the reports published^{61,69}. The metal-metal bonding (Au-Sc) within the octahedral can also have a metallic character due to the overlap of their atomic orbitals.

The combination of ionic, covalent, and metallic bonding interactions influences the charge density distribution in materials. The A ions contribute to the charge density by providing localized positive charge, while the X ions contribute localized negative charge due to electronegativity. In summary, the charge density and bonding nature of A_2AuScX_6 (A= Cs/Rb; X= Cl/Br/I) result from the complex interplay between ionic, covalent, and metallic bonding interactions within its crystal structure. This unusual bonding is the key to many of their desirable photovoltaic properties.

3.4. Optical properties

Optical characteristics reflect electronic properties and indicate how a material reacts to incident light. Photon energy in the region of 0 to 14 eV is used to study optical constants such as dielectric function, refraction index, absorption coefficient, and reflectivity and photoelectric/device applications of these DP materials. Their absorption coefficients and the material's electric polarization performance are the primary features of the photovoltaic application.

The complex dielectric function may be represented by the real and imaginary components of the dielectric function with respect to photon energy, which is given by the following formula: $\epsilon(\omega) = \epsilon_1(\omega) + i\epsilon_2(\omega)$

The real portion of $\epsilon_1(\omega)$ indicates the amount of polarization when the external field is applied, can be calculated by the equations of Kramers-Kronig⁷⁰, while $\epsilon_2(\omega)$ indicates an amount of

electronic change or light absorption and can be calculated by Kohn-Shams⁷¹ equation, respectively.

$$\varepsilon_1(\omega) = 1 + \frac{2}{\pi} P \int_0^{\infty} \frac{\omega' * \varepsilon_2(\omega')}{\omega'^2 - \omega^2} d\omega$$

$$\varepsilon_2(\omega) = \frac{Ve^2}{2\pi\hbar m^2 \omega^2} \int d^3k \sum_{nn'} |(kn|p|kn')|^2 f(kn) \times (1 - f(kn')) \delta(E_{kn} - E_{kn'} - \hbar\omega)$$

Where P in the first equation stands for the main component, the 2nd equation uses V, e, \hbar , p, kn, and kn' to represent unit volume, charge, decreasing plank constant, momentum transfer matrix, VB wave function, and CB wave function.

The dielectric function of the mentioned DP of A₂AuScX₆ is shown in Fig.6 (a and b). The real part of the dielectric constant $\varepsilon_1(\omega)$ first experienced a dramatic increase until it reached its maximum value, after which it began a downward trend. The static dielectric constants are 3.27 (3.19), 3.84 (3.76), and 4.97 (4.90) for A₂AuScX₆ [A = Cs, Rb; X = Cl, Br, I], and the highest value is seen to be 6.06 (6.03) at 2.33 (2.37) eV, 6.39 (6.36) at 2.22 (2.25) eV, and 7.70 (7.67) at 1.85 (1.89) eV for A₂AuScX₆ [A = Cs, Rb; X = Cl, Br, I], respectively. The compounds of Cs-based halide display slightly greater dielectric behavior (static or dynamic) than Rb-based halide. The minimal variation in $\varepsilon_1(\omega)$ for all compounds under study is, however, within -1.16 to -2 for energies greater than 10 eV, where the minus sign of $\varepsilon_1(\omega)$ indicates the compound's metallic character. Also, it was found that switching Cl with Br and I, elevated the strength of the peaks of absorption and pushed them to a smaller energy region since I has a bigger electronic influence than Br and Cl. The static polarization and band gap are linked inversely by the Penn's model⁷²:

$$\varepsilon_1(0) \approx 1 + \left[\frac{\hbar\omega_p}{E_g} \right]^2$$

Where \hbar and ω_p are the decreased plank constant and the frequency of the plasma, respectively.

The $\varepsilon_2(\omega)$ is significant because it determines the maximum absorption area and governs interband transitions that take place inside the materials used to fabricate devices. Due to the limitations of DFT, the transition points (VB to CB) exhibit a slight deviation from band structure and are plotted in Fig.6(b). The maximum value of ε_2 is called generally the first

absorption peak (FAP) and is responsible for the electronic transition at the Fermi level. In the case of $A_2AuScCl_6$ (A= Cs/Rb), the FAP is 2.71 and 2.79 eV, respectively. The remaining compounds have various peaks in the range of 4 eV, which were seen for $A_2AuScBr_6$ (A= Cs, Rb) at 2.54 (2.56) and 2.83 (2.88) eV and for A_2AuScI_6 (A= Cs/Rb) at 2.27 (2.30), 2.79 (2.88), and 3.29 (3.35) eV, respectively. For the titled compounds, we simply need to know the highest FAP values, which are 2.71 (2.79) eV, 2.54 (2.56 eV), and 2.27 (2.30) eV for A_2AuScX_6 [A = Cs, Rb; X = Cl, Br, I], respectively. These values are in the visible range and indicate an effective absorption capacity. Compared to the DOS, the FAS originates mainly by the Au-*d* along with X-*p* at MVB (Maximum of VB) and the Sc-*d* at MCB (Minimum of CB) point.

The absorption capacity $\alpha(\omega)$, is comparable to that of $\varepsilon_2(\omega)$ also illustrated by their coefficients at various energies (photon energy) and wavelength, as shown in Fig. 6(c) and Fig. 6(d). The formula for the absorption coefficient $\alpha(\omega)$ was derived from the imaginary and real parts of the dielectric function⁶⁸.

$$\alpha(\omega) = 2\omega \left(\frac{[\varepsilon_1^2(\omega) + \varepsilon_2^2(\omega)]^{1/2} - \varepsilon_1(\omega)}{2} \right)^{1/2}$$

The absorption edge, also known as the optical band gap or resultant value $\alpha(\omega)$ of the material precisely corresponds to the electronic band gap, and the first highest absorption is observed at 2.95 (3.07), 2.67 (2.72), and 2.34 (2.36) eV for A_2AuScX_6 [A = Cs, Rb; X = Cl, Br, I], respectively, which are in the visible range. Therefore, these DPs function well as absorbents for the visible spectrum. Other maximum absorption peaks, which also lie in the visible to UV range, are found at 2.67 (2.72) and 3.03 (3.07) eV for $A_2AuScBr_6$ (A= Cs/Rb) and 2.34 (2.36), 3.11 (3.16) eV, and 3.36 (3.42) eV for A_2AuScI_6 (A= Cs/Rb). The development of several peaks with various peak intensities in the upper range from 7 to 13 eV illustrates the various possibilities of transition from filled to unfilled states.

Besides, these materials have superior absorption coefficients than others, such as 3 to 6.5×10^4 cm^{-1} for Cs_2CuBiX_6 (X= Cl/Br/I)⁷³, 4.8 to 5×10^4 cm^{-1} for Rb_2CuBiX_6 (X= Cl/Br)⁷⁴, 5 to 5.3×10^4 cm^{-1} for K_2CuBiX_6 (X= Cl/Br)⁷⁵ and 8×10^4 cm^{-1} for Cs_2AgBiI_6 ⁷⁶, according to the highest peaks of both compounds, which are situated at wavelength of visible range (400-700nm). The visible range absorption coefficients for $A_2AuScCl_6$ (A= Cs/Rb) is 3.33 (3.45) $\times 10^5$ cm^{-1} . Other compounds show the different highest peak in the visible to UV range, for instance,

$A_2AuScBr_6$ (A= Cs/Rb) is 2.20 (2.24) $\times 10^5$ cm^{-1} and 2.70 (2.81) $\times 10^5$ cm^{-1} , and A_2AuScI_6 (A= Cs/Rb) is 2.13 (2.18) $\times 10^5$ cm^{-1} , 3.17 (3.20) $\times 10^5$ cm^{-1} and 4.46 (4.55) $\times 10^5$ cm^{-1} , respectively. Due to their excellent photoelectric defining features, these DP halide materials might be employed as the layer that absorbs sunlight in solar cells.

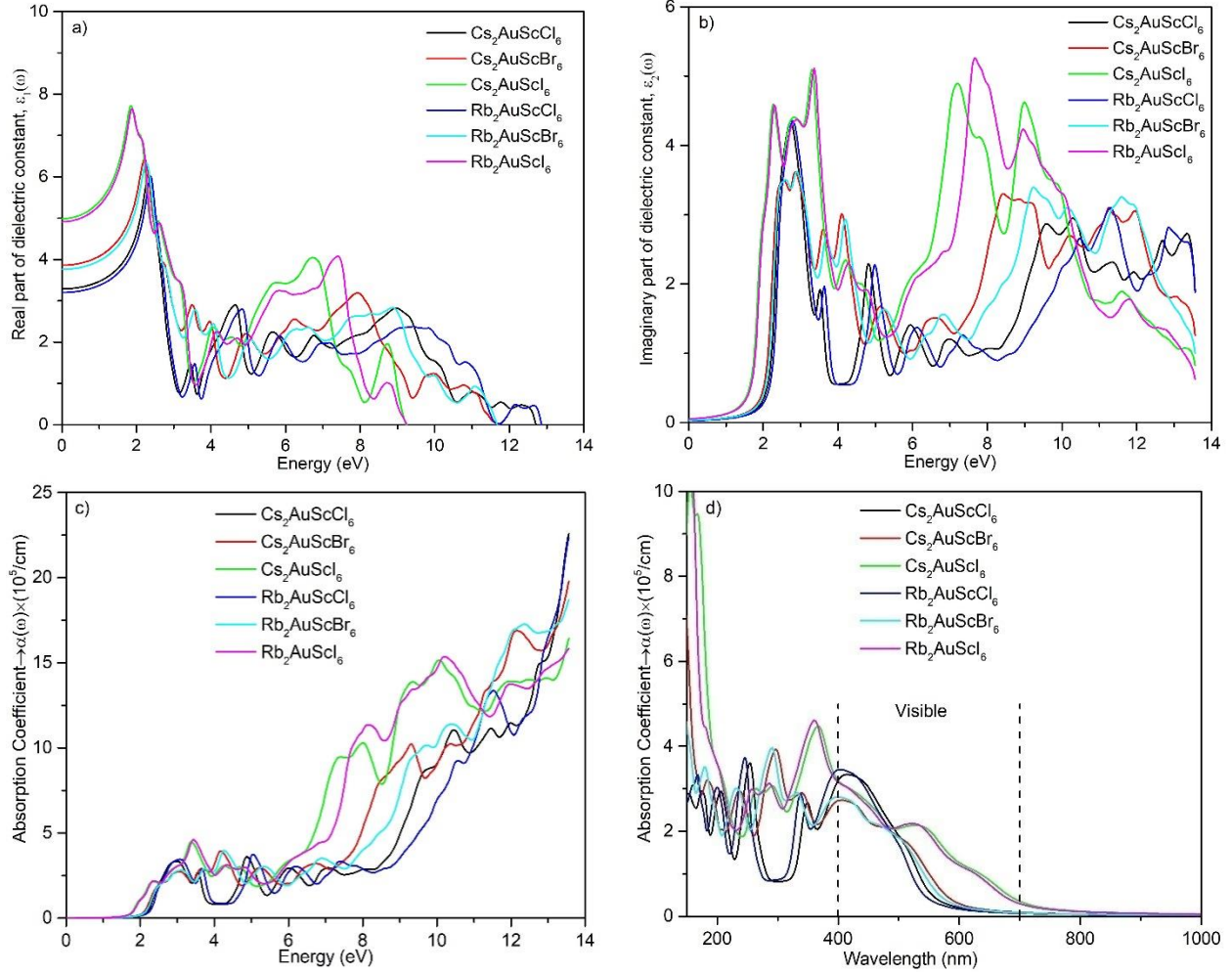


Fig.6: Obtained values of a) real part of the dielectric constant, b) imaginary part of the dielectric constant, c) absorption coefficient in eV and d) absorption coefficient in nm for DP of $Cs_2AuScCl_6$, $Cs_2AuScBr_6$, Cs_2AuScI_6 , $Rb_2AuScCl_6$, $Rb_2AuScBr_6$, and Rb_2AuScI_6 .

Other essential optical constants, such as the refractive factor $n(\omega)$, the extinction factor $k(\omega)$, the reflectivity $R(\omega)$, and loss factor $L(\omega)$, are all calculated from the dielectric properties of all compounds^{77, 78, 79}.

$$n(\omega) = \left[\frac{\{\epsilon_1^2(\omega) + \epsilon_2^2(\omega)\}^{1/2}}{2} + \frac{\epsilon_1(\omega)}{2} \right]^{1/2}$$

$$k(\omega) = \left[\frac{\{\varepsilon_1^2(\omega) + \varepsilon_2^2(\omega)\}^{1/2}}{2} - \frac{\varepsilon_1(\omega)}{2} \right]^{1/2}$$

$$R(\omega) = \frac{\{n(\omega) - 1\}^2 + k^2(\omega)}{\{n(\omega) + 1\}^2 + k^2(\omega)}$$

$$L(\omega) = \frac{\varepsilon_2}{\varepsilon_1^2 + \varepsilon_2^2}$$

The refractive index calculation results are displayed in Fig.7(a). The link between $n^2(\omega) = \varepsilon_1(\omega)$ caused the real part of the dielectric function and refractive index to behave in the same way⁸⁰. The static refractive factors of $n(0)$ are 1.81 (1.79), 1.96 (1.93) and 2.22 (2.20), and their maximum values are 2.49 (2.48), 2.57 (2.53) and 2.80 (2.78), with 2.28 (2.37) eV, 2.20 (2.28) eV, and 1.84 (1.87) eV, for A_2AuScX_6 ; A= Cs/Rb, X= Cl/Br/I, respectively. Optoelectronic activities are appropriate for $n(\omega)$ values from 2.0 to 4.0⁸¹, and the studied materials have values within this range. The fact that the observed refractive factor values are more than 1 is strong evidence for semiconducting materials. The refractive factor also evaluates the strength of the bonds—whether they are more or less than unity. A refractive index greater than one indicates the presence of covalent bonds rather than ionic ones. Due to photon slowing and increasing electron density, the aforementioned materials displayed covalent bonding, either static or dynamic³⁷.

Table 4: Computed optical constants.

| Compound | $\varepsilon_1(0)$ | $n(0)$ | $R(0)$ |
|-----------------|--------------------------------------|--------------------------|--------------------------|
| $Cs_2AuScCl_6$ | 3.27 | 2.22 | 8.37% |
| $Cs_2AuScBr_6$ | 3.85 | 1.96 | 10.70% |
| Cs_2AuScI_6 | 4.98 | 1.81 | 14.58% |
| $Rb_2AuScCl_6$ | 3.19 | 2.20 | 7.96% |
| $Rb_2AuScBr_6$ | 3.74 | 1.93 | 10.19% |
| Rb_2AuScI_6 | 4.90 | 1.79 | 14.07% |

The identical pattern of $\varepsilon_2(\omega)$ and $\alpha(\omega)$ is followed by the extinction factor $k(\omega)$, which detects the loss of EM waves in contents, as shown in Fig.7(b). The connection between $k(\omega)$ and $\alpha(\omega)$ is as follows:

$$k = \frac{\alpha\lambda}{4\pi}$$

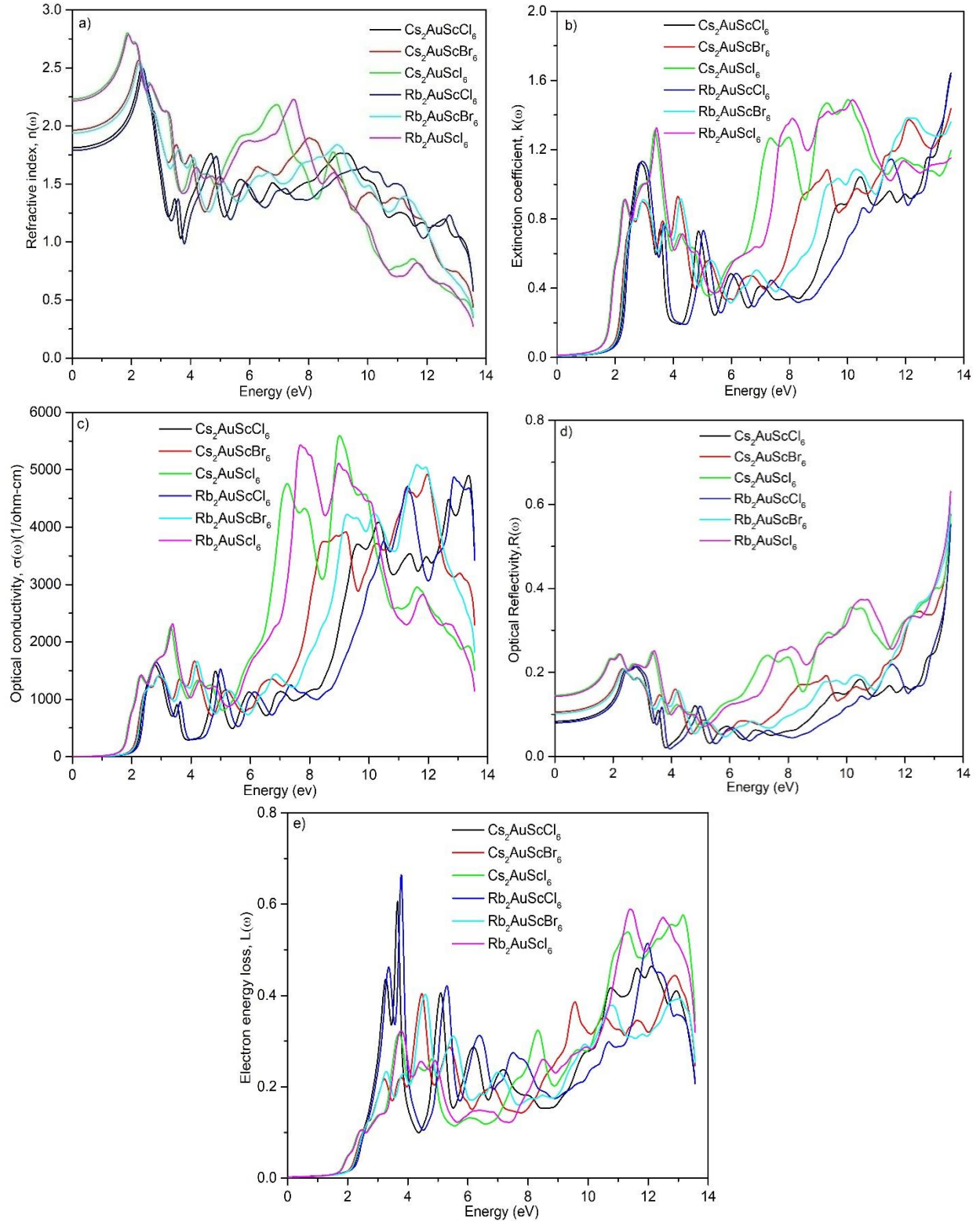


Fig.7: The obtained a) refractive index, b) extinction coefficient, c) optical conductivity d) optical reflectivity, and e) electron energy loss of $\text{Cs}_2\text{AuScCl}_6$, $\text{Cs}_2\text{AuScBr}_6$, $\text{Cs}_2\text{AuScI}_6$, $\text{Rb}_2\text{AuScCl}_6$, $\text{Rb}_2\text{AuScBr}_6$, and $\text{Rb}_2\text{AuScI}_6$.

The value of the extinction coefficient was discovered to be extremely low, as would be predicted for semiconductor materials⁸². Any material's surface will absorb some of the incident light if a stream of photons at a specific frequency strikes it, initiating the interband transition or switching of electrons. The amount of real optical conductivity is used to measure this change. For optoelectronic devices to function practically, the optical conductivity, which is determined by the interband movement of electrons, must be within 1.4 to 4.0 eV in the visible range⁸¹. The initial peak exhibits maximum conductivities of 1594/1637 ($\Omega\text{-cm}$)⁻¹ at 2.71/2.81 eV for $A_2\text{AuScCl}_6$ (A= Cs/Rb), 1227/1247 ($\Omega\text{-cm}$)⁻¹ at 2.58/2.64 eV and 1401/1412 ($\Omega\text{-cm}$)⁻¹ at 2.88/2.90 eV for $A_2\text{AuScBr}_6$ (A= Cs/Rb), and 1402/1417 ($\Omega\text{-cm}$)⁻¹ at 2.29/2.31 eV, 1749/1755 ($\Omega\text{-cm}$)⁻¹ at 2.99/3.01 eV and 2266/2299 ($\Omega\text{-cm}$)⁻¹ at 3.29/3.35 eV for $A_2\text{AuScI}_6$ (A= Cs/Rb), respectively, while the highest value observed (4100 to 5500 1/ $\Omega\text{-cm}$) from 7 to 13 eV, as shown in Fig. 7(c).

The static value of reflectivity is less than 15% for the explored compounds. The lowest reflectivity $R(\omega)$ indicates that both materials are thought to be more effective for incoming light, with energy values ranging from zero to the gap in the band, as shown in Fig.7(d). The computed value of $L(\omega)$ measures the amount of energy (less than 0.3 in the visible range) that disappears when a photon travels through a substance, as shown in Fig.7(e). A very low reflectivity and loss function value is significant for the materials to be used as absorbing layers in solar cells. Finally, these materials can be used in optoelectronic gadgets because of their adjustable computing band gap, strong dielectric strength, excellent absorbance spectra, and good photoconductivity.

3.5. Thermoelectric properties

Given the increasing demand for energy, waste heat recovery—a method that transforms heat into electrical energy—becomes increasingly important in systems to improve material efficiency. Thermoelectric (TE) materials produce portable power for distant missions, energy devices, and cooling applications. An analysis of a compound's transport properties is necessary to determine whether it is appropriate for these uses. For the materials under study, effective thermoelectric conversion requires reducing heat conductivity (κ) and increasing electrical conductivity (σ). The See-beck coefficient (S), power factor (PF), and figure of merit (ZT) would

all rise as a result of this. Additional information, such as a smaller band gap and greater carrier mobility must be considered when analyzing TE materials.

These materials' electronic band structure and phonons' dispersion—vibrations that move heat across the lattice—determine their thermoelectric (TE) properties. Lattice thermal vibrations (K_L) are calculated in the thermo-mechanical section (supplementary data, Table S1).

To calculate the TE behavior with respect to temperature, we employ the Boltzmann transport theory⁸³. Specifically, we utilize the Boltztrap2 code⁴⁵ for integrating Fermi energy, a process dependent on the concentration of both n and p-type charge carriers. Additionally, we incorporate the electronic components of thermal conductivity (K_e) and electrical conductivity (σ) into the calculation, considering a relaxation time ($\tau = 10^{-14}$ s).

Table 5: Room temperature computed values of electrical conductivity (σ), electronic conductivity (K_e), See-beck coefficient (S), power factor (PF), and figure of merit (ZT) of the investigated compounds.

| Compound | σ ($\times 10^5$ /Ω.m) | K_e ($\times 10^{14}$ Wm⁻¹K⁻¹) | S (mV/K) | PF ($\times 10^{-3}$ Wm⁻¹K⁻²) | ZT |
|-------------------------------------|--|---|-----------------|---|-----------|
| Cs ₂ AuScCl ₆ | 1.06 | 0.43 | 0.192 | 3.98 | 0.92 |
| Cs ₂ AuScBr ₆ | 0.90 | 0.37 | 0.211 | 4.03 | 1.07 |
| Cs ₂ AuScI ₆ | 0.87 | 0.37 | 0.213 | 4.01 | 1.06 |
| Rb ₂ AuScCl ₆ | 1.01 | 0.41 | 0.199 | 4.02 | 0.97 |
| Rb ₂ AuScBr ₆ | 0.90 | 0.39 | 0.208 | 3.92 | 0.99 |
| Rb ₂ AuScI ₆ | 0.92 | 0.39 | 0.209 | 4.06 | 1.01 |

Electrical conductivity (σ) measures how well a material conducts electricity. The initial electrical conductivity values at 200K for Cs₂AuScX₆ (Rb₂AuScX₆), where X represents Cl, Br, or I, are 0.73 (0.66) $\times 10^5$, 0.56 (0.55) $\times 10^5$, and 0.54 (0.57) $\times 10^5$ (1/ Ω .m), respectively. A key feature of semiconductors is that all compounds increase electrical conductivity with temperature⁸⁴. Moreover, the I-based compound outperforms the Br and Cl-based compounds, achieving the greatest conductivity values as the temperature becomes closer to its maximum range of 200 to 1000K, as shown in Fig. 8(a). This is explained by the fact that more bonds are broken in halides based on Cs and Rb. The electrical conductivity values that were measured at

high temperatures (1000K) are 2.27 (2.29), 2.38 (2.39), and 2.53 (2.58) $\times 10^5$ ($1/\Omega.m$) for $Cs_2AuScCl_6$ ($Rb_2AuScCl_6$), $Cs_2AuScBr_6$ ($Rb_2AuScBr_6$), and Cs_2AuScI_6 (Rb_2AuScI_6), respectively.

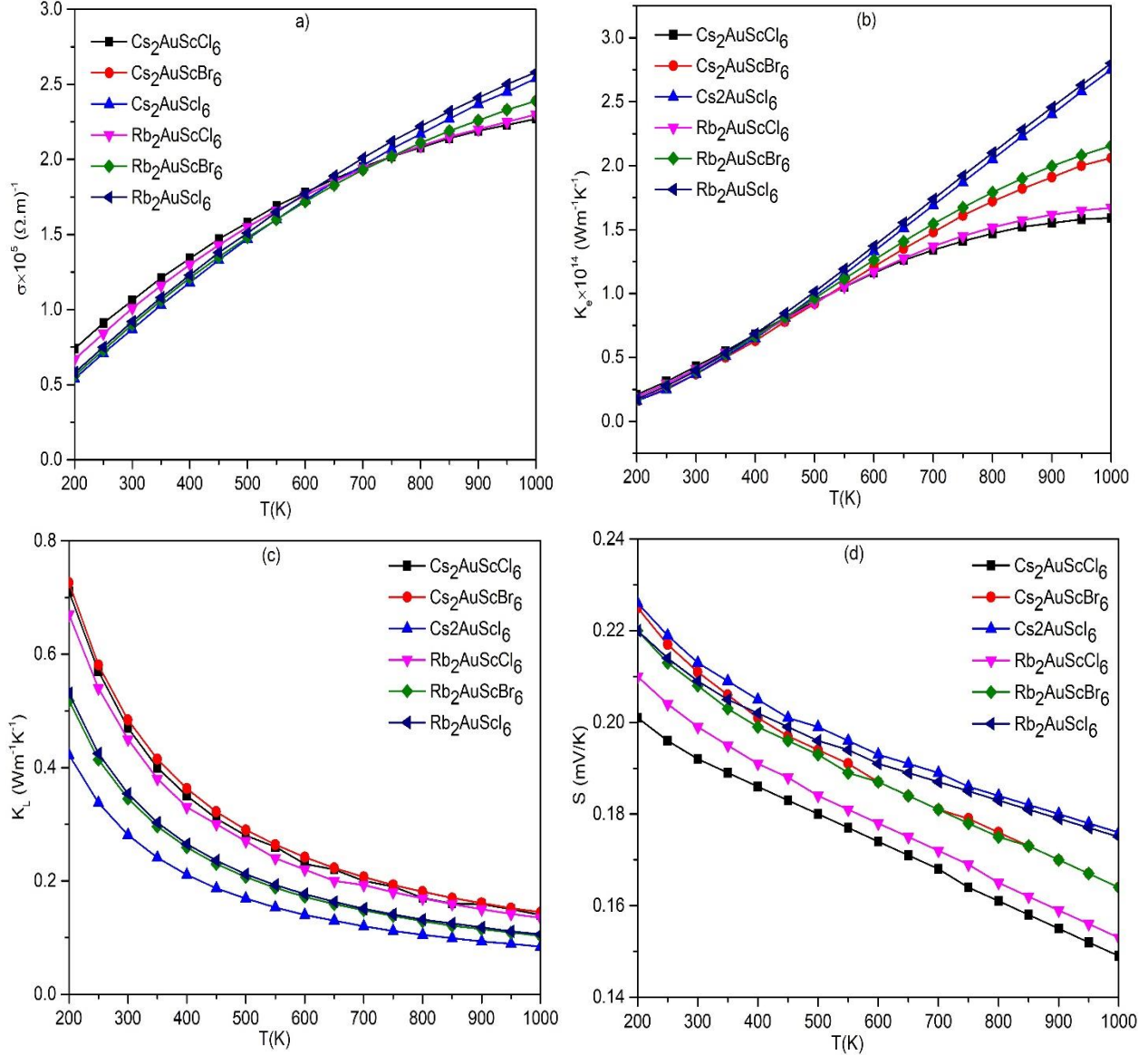


Fig.8: The computed a) Electrical conductivity, σ , b) Electronic part of thermal conductivity, K_e , c): Lattice thermal conductivity (from supplementary part) K_L , and d) See-beck coefficient, S , of the studied compounds.

The trends in the graphs of K_e and σ versus temperature (T) are roughly the same. The electronic conductivity increases with temperature. As can be seen in Fig. 8(b), the highest values of 1.58 (1.66), 2.05 (2.15), and 2.75 (2.79) $Wm^{-1}K^{-1}$ are obtained at $1000K$ for $Cs_2AuScCl_6$

($\text{Rb}_2\text{AuScCl}_6$), $\text{Cs}_2\text{AuScBr}_6$ ($\text{Rb}_2\text{AuScBr}_6$), $\text{Cs}_2\text{AuScI}_6$ ($\text{Rb}_2\text{AuScI}_6$), respectively. The low thermal conductivity (κ), which is the sum of K_L and K_e ^{85,86}, and high σ values of these materials make them appropriate for thermoelectric applications. Table 5 provides the computed parameters for σ , K_e , and K_L at room temperature (300K). Interestingly, their electrical conductivity (σ) is a factor of 10^5 higher than their heat conductivity (K_e), highlighting their considerable potential for optoelectronic applications.

When applying a temperature gradient, the See-beck coefficient (S) measures the voltage produced across a material. In thermoelectric materials, a high See-beck coefficient is highly desirable⁸⁷. Notably, the See-beck coefficient decreases as the temperature rises. In the case of Cs (Rb)-based compositions containing Cl, Br, and I atoms, the S values decrease from 0.201 to 0.149 (0.231 to 0.152) mV/K, 0.224 to 0.163 (0.249 to 0.164) mV/K, and 0.226 to 0.175 (0.243 to 0.174) mV/K, respectively, over the temperature range of 200 to 1000K, as displayed in Fig.8(d). The S values observed at 300K are given in Table 5 and exhibit the following trend: $\text{Cs}_2\text{AuScI}_6 > \text{Cs}_2\text{AuScBr}_6 > \text{Cs}_2\text{AuScCl}_6$ for Cs-based halides and $\text{Rb}_2\text{AuScI}_6 > \text{Rb}_2\text{AuScBr}_6 > \text{Rb}_2\text{AuScCl}_6$ for Rb-based halides. Because these compounds have positive S values within the designated temperature range are classified as P-type.

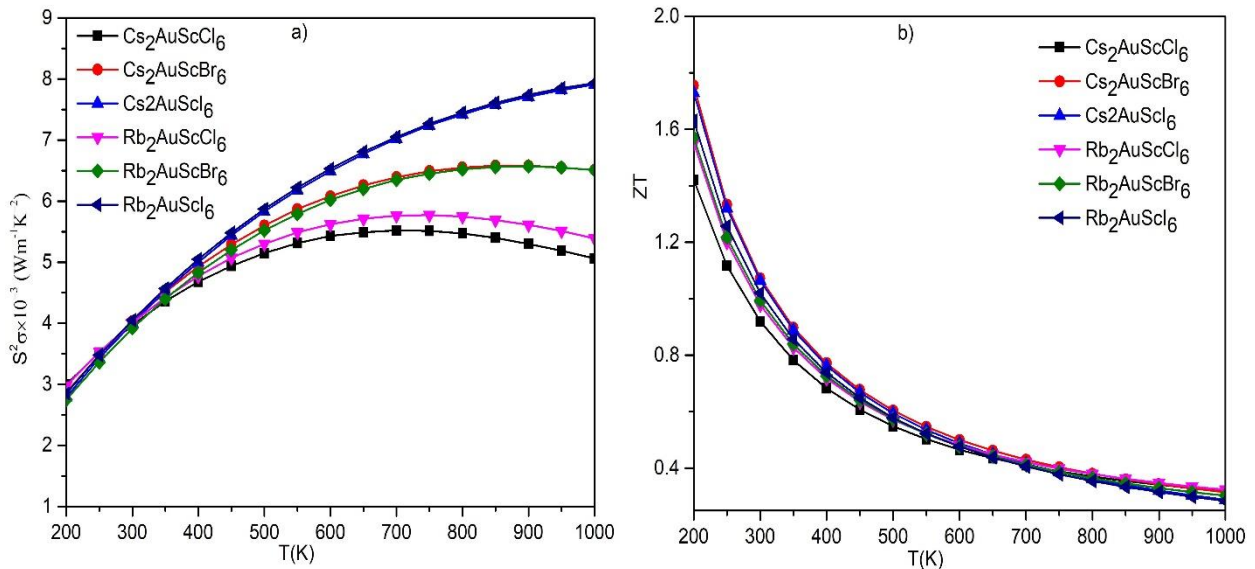


Fig.9: a) Power factor (PF) $S^2\sigma$ and b) Figure of merit (ZT) of the studied compounds.

One of the most important factors in assessing a material's TE characteristics is its power factor. It measures how well a thermoelectric material transforms heat into electrical power. In

mathematics, the power factor is defined as⁸⁸: $PF = S^2\sigma$, where S represents the Seebeck coefficient, also known as thermo-power or thermoelectric voltage, and σ denotes the electrical conductivity. The graph illustrating PF versus temperature (T) can be seen in the Fig.9 (a). As temperature increases, the power factor also rises, reaching its peak values of $5.51 \text{ Wm}^{-1}\text{K}^{-2}$, $6.55 \text{ Wm}^{-1}\text{K}^{-2}$, and $7.88 \text{ Wm}^{-1}\text{K}^{-2}$ at 700K, 800K, and 1000K for $\text{Cs}_2\text{AuScCl}_6$, $\text{Cs}_2\text{AuScBr}_6$, and $\text{Cs}_2\text{AuScI}_6$, respectively. For $\text{Rb}_2\text{AuScCl}_6$, $\text{Rb}_2\text{AuScBr}_6$, and $\text{Rb}_2\text{AuScI}_6$, the corresponding values are $5.76 \text{ Wm}^{-1}\text{K}^{-2}$, $6.54 \text{ Wm}^{-1}\text{K}^{-2}$, and $7.90 \text{ Wm}^{-1}\text{K}^{-2}$ at 700K, 800K, and 1000K, respectively. However, the studied compounds have higher PF at room temperature than some known TE materials, such as 2.64 and 2.61 for $\text{Tl}_2(\text{Se}, \text{Te})\text{Cl}_6$ ⁸⁹.

The ZT value is a dimensionless figure of merit that assesses the effectiveness of the TE materials in association with the aforementioned characteristics. Measurement of the dimensionless figure of merit is used to measure thermoelectric material efficiency. ZT is defined as $ZT = \frac{s^2\sigma}{\kappa}T$, where κ is the thermal conductivity made up of the electronic and lattice parts, σ is the electrical conductivity, and S is the thermo-power. Promising TE materials are those with a high $ZT \sim 1.0$, which may be attained when the power factor $s^2\sigma$ is high, and the thermal conductivity is low⁹⁰. Nevertheless, it is important to remember that a rise in temperature causes the ZT value to decrease. As seen in Fig. 9(b), the ZT values at 300K for compositions based on Cs and including Cl, Br, and I atoms are 0.92, 1.07, and 1.06, respectively, whereas for compositions based on Rb and containing Cl, Br, and I atoms, they are 0.97, 0.99, and 1.01, respectively. So these materials show higher ZT values compared with other DP halide such as 0.77, 0.82, and 0.95 for $\text{Rb}_2\text{ScTlX}_6$ ($X = \text{Cl}, \text{Br}, \text{I}$)⁸¹, 0.63, 0.61, and 0.66 for $\text{Cs}_2\text{ScTlX}_6$ ($X = \text{Cl}, \text{Br}, \text{I}$)³⁸, 0.61, 0.72, and 0.81 for Cs_2KTlX_6 ($X = \text{Cl}, \text{Br}, \text{I}$)⁹¹, 0.76 to 0.78 for $\text{Rb}_2\text{AlInX}_6$ ($X = \text{Cl}, \text{Br}, \text{I}$)⁹² and the most studied DP halide is about 0.86 and 0.84, for $\text{Cs}_2\text{AgBiX}_6$ ($X = \text{Cl}, \text{Br}$)⁹³. Also, the studied two halides, $\text{Cs}_2\text{AuScBr}_6$ and $\text{Cs}_2\text{AuScI}_6$, can be considered more promising TE materials ($ZT = 1.07$ and 1.06) than Cs_2PtI_6 ($ZT = 1.03$)⁸⁵ due to high Seebeck coefficient values at room temperature. Therefore, the studied DP materials could fulfill the necessity for waste heat use and sustainable energy solutions.

4. Conclusion

The ground state structure is obtained for the titled compounds by the DFT calculations with the aid of the Wien2k code. The structural stability is confirmed by the formation energy, binding energy, phonon dispersion curve, stiffness constants, tolerance, and octahedral factors. The lattice constants increase from 10.44 to 11.89 Å when Br and I replace the Cl ion. The electronic band structure confirms the semiconducting nature. Using the TB mBJ potential, the energy band gaps of $A_2AuScCl_6$ (A= Cs/Rb), $A_2AuScBr_6$ (A= Cs/Rb), and A_2AuScI_6 (A= Cs/Rb) are 1.88 (1.93), 1.68 (1.71), and 1.30 (1.32) eV, respectively. The band gap values of the DP of the titled compounds are close to the S. Q. limit⁹⁴ for maximum efficiency, which makes them suitable for application in solar cell devices. The lowest effective mass of an electron and a hole that satisfies green or sustainable energy technology. The DOS and charge density mapping plots explore the bonding nature present within the studied materials. The important optical constants demonstrate the studied material's response to the incident photon. The usefulness of the titled compounds in optoelectronic applications stems from their high absorption coefficients of 10^5 order and other optical constants, including low energy loss and reflection capacity (reflectivity is less than 15%). The DPs, A_2AuScX_6 (A= Cs, Rb; X= Cl, Br, I), are, therefore, promising options for efficient solar cells and reasonably priced optoelectronic devices because of their strong light absorption capacity and remarkable adjustable band gap. Analysis of thermoelectric properties reveals essential prospects for the titled compounds. The reduced lattice thermal conductivity and band gap values confirm their usage in thermoelectric devices. The high ZT values of 0.92, 1.07, 1.06, 0.97, 0.99, and 1.01 calculated power factor and thermal conductivity at 300K for $Cs_2AuScCl_6$, Cs_2AuBr_6 , Cs_2AuScI_6 , $Rb_2AuScCl_6$, $Rb_2AuScBr_6$, and Rb_2AuScI_6 , respectively imply that studied compounds are promising thermoelectric materials. The elastic properties certify the ductility that confirms the studied compound's machinability, which is essential for device fabrication. Moreover, high melting points and low K_{min} values also support their high-temperature use. In the end, the obtained results of the titled DPs are encouraging and hope to provide proper guidance for future research on energy harvesting materials.

Declaration of interests

The authors declare that they have no known competing financial interests or personal relationships that could have appeared to influence the work reported in this paper.

Acknowledgments

This work was carried out with the aid of a grant (grant number: 21-378 RG/PHYS/AS_G - FR3240319526) from UNESCO-TWAS and the Swedish International Development Cooperation Agency (SIDA). The views expressed herein do not necessarily represent those of UNESCO-TWAS, SIDA or its Board of Governors.

CRedit Author contributions

S. Mahmud: Conceptualization, Formal analysis, Methodology, Data calculations, Validation, Writing – original draft. **M.A.Ali:** Conceptualization, Methodology, Formal analysis, Validation, Project administration, Writing – original draft, Supervision. **M.M. Hossain:** Writing – review & editing, Validation. **M.M. Uddin:** Writing – review & editing, Validation.

References

1. Yin WJ, Weng B, Ge J, Sun Q, Li Z, Yan Y. Oxide perovskites, double perovskites and derivatives for electrocatalysis, photocatalysis, and photovoltaics. *Energy & Environ Sci.* 2019;12(2):442-462.
2. Kung PK, Li MH, Lin PY, et al. Lead-free double perovskites for perovskite solar cells. *Sol RRL.* 2020;4(2):1900306.
3. Dar SA, Want B. Direct band gap double perovskite halide Cs₂ScInCl₆ for optoelectronic applications—A first principle study. *Comput Condens Matter.* 2022;33:e00736.
4. Kaltzoglou A, Antoniadou M, Kontos AG, et al. Optical-vibrational properties of the Cs₂SnX₆ (X= Cl, Br, I) defect perovskites and hole-transport efficiency in dye-sensitized solar cells. *J Phys Chem C.* 2016;120(22):11777-11785.
5. Savory CN, Walsh A, Scanlon DO. Can Pb-free halide double perovskites support high-efficiency solar cells? *ACS energy Lett.* 2016;1(5):949-955.
6. Chen J, Cai X, Yang D, et al. Recent progress in stabilizing hybrid perovskites for solar cell applications. *J Power Sources.* 2017;355:98-133.
7. Lee B, Stoumpos CC, Zhou N, et al. Air-stable molecular semiconducting iodosalts for solar cell applications: Cs₂SnI₆ as a hole conductor. *J Am Chem Soc.* 2014;136(43):15379-15385.
8. Maughan AE, Ganose AM, Bordelon MM, Miller EM, Scanlon DO, Neilson JR. Defect tolerance to intolerance in the vacancy-ordered double perovskite semiconductors Cs₂SnI₆ and Cs₂TeI₆. *J Am Chem Soc.* 2016;138(27):8453-8464.
9. Fang MJ, Tsao CW, Hsu YJ. Semiconductor nanoheterostructures for photoconversion applications. *J Phys D Appl Phys.* 2020;53(14):143001.

10. Kumar M, Raj A, Kumar A, Anshul A. Theoretical evidence of high power conversion efficiency in double perovskite solar cell device. *Opt Mater (Amst)*. 2021;111:110565.
11. Tang H, Xu Y, Hu X, et al. Lead-Free Halide Double Perovskite Nanocrystals for Light-Emitting Applications: Strategies for Boosting Efficiency and Stability. *Adv Sci*. 2021;8(7):2004118.
12. Kurtz S, Repins I, Metzger WK, et al. Historical analysis of champion photovoltaic module efficiencies. *IEEE J Photovoltaics*. 2018;8(2):363-372.
13. Seok S Il, Grätzel M, Park NG. Methodologies toward highly efficient perovskite solar cells. *Small*. 2018;14(20):1704177.
14. Park J, Kim J, Yun HS, et al. Controlled growth of perovskite layers with volatile alkylammonium chlorides. *Nature*. 2023;616(7958):724-730.
15. Zhou J, Huang J. Photodetectors based on organic--inorganic hybrid lead halide perovskites. *Adv Sci*. 2018;5(1):1700256.
16. Chen Q, De Marco N, Yang YM, et al. Under the spotlight: The organic--inorganic hybrid halide perovskite for optoelectronic applications. *Nano Today*. 2015;10(3):355-396.
17. Zhao XG, Yang D, Ren JC, Sun Y, Xiao Z, Zhang L. Rational design of halide double perovskites for optoelectronic applications. *Joule*. 2018;2(9):1662-1673.
18. Chu L, Ahmad W, Liu W, et al. Lead-free halide double perovskite materials: a new superstar toward green and stable optoelectronic applications. *Nano-Micro Lett*. 2019;11:1-18.
19. Bibi A, Lee I, Nah Y, et al. Lead-free halide double perovskites: Toward stable and sustainable optoelectronic devices. *Mater Today*. 2021;49:123-144.
20. Cai B, Chen X, Xie M, et al. A class of Pb-free double perovskite halide semiconductors with intrinsic ferromagnetism, large spin splitting and high Curie temperature. *Mater Horizons*. 2018;5(5):961-968.
21. Khawar S, Afzal MQ, Husain M, et al. First-principles calculations to investigate structural, electronic, optical, and magnetic properties of a scintillating double perovskite halide ($\text{Cs}_2\text{LiCeCl}_6$). *J Mater Res Technol*. 2022;21:4790-4798.
22. Radja K, Farah BL, Ibrahim A, et al. Investigation of structural, magneto-electronic, elastic, mechanical and thermoelectric properties of novel lead-free halide double perovskite $\text{Cs}_2\text{AgFeCl}_6$: First-principles calculations. *J Phys Chem Solids*. 2022;167:110795.
23. Xu X, Zhong Y, Shao Z. Double perovskites in catalysis, electrocatalysis, and photo (electro) catalysis. *Trends Chem*. 2019;1(4):410-424.
24. Zhang Z, Liang Y, Huang H, et al. Stable and highly efficient photocatalysis with lead-free double-perovskite of $\text{Cs}_2\text{AgBiBr}_6$. *Angew Chemie Int Ed*. 2019;58(22):7263-7267.
25. Hu R, Ding R, Chen J, Hu J, Zhang Y. Preparation and catalytic activities of the novel double perovskite-type oxide $\text{La}_2\text{CuNiO}_6$ for methane combustion. *Catal Commun*.

- 2012;21:38-41.
26. Kale AJ, Chaurasiya R, Dixit A. Lead-Free Cs₂BB'X₆ (B: Ag/Au/Cu, B': Bi/Sb/Tl, and X: Br/Cl/I) Double Perovskites and Their Potential in Energy Conversion Applications. *ACS Appl Energy Mater.* 2022;5(9):10427-10445.
 27. Noor NA, Iqbal MW, Zelai T, et al. Analysis of direct band gap A₂ScInI₆ (A= Rb, Cs) double perovskite halides using DFT approach for renewable energy devices. *J Mater Res Technol.* 2021;13:2491-2500.
 28. Aslam F, Ullah H, Hassan M. Theoretical investigation of Cs₂InBiX₆ (X= Cl, Br, I) double perovskite halides using first-principle calculations. *Mater Sci Eng B.* 2021;274:115456.
 29. Kobayashi KI, Kimura T, Sawada H, Terakura K, Tokura Y. Room-temperature magnetoresistance in an oxide material with an ordered double-perovskite structure. *Nature.* 1998;395(6703):677-680.
 30. Yáñez-Vilar S, Mun ED, Zapf VS, et al. Multiferroic behavior in the double-perovskite Lu₂MnCoO₆. *Phys Rev B.* 2011;84(13):134427.
 31. Jeon BC, Kim CH, Moon SJ, et al. Electronic structure of double perovskite A₂FeReO₆ (A= Ba and Ca): interplay between spin-orbit interaction, electron correlation, and lattice distortion. *J Phys Condens Matter.* 2010;22(34):345602.
 32. Slavney AH, Hu T, Lindenberg AM, Karunadasa HI. A bismuth-halide double perovskite with long carrier recombination lifetime for photovoltaic applications. *J Am Chem Soc.* 2016;138(7):2138-2141.
 33. Tariq M, Ali MA, Laref A, Murtaza G. Anion replacement effect on the physical properties of metal halide double perovskites Cs₂AgInX₆ (X= F, Cl, Br, I). *Solid State Commun.* 2020;314:113929.
 34. McClure ET, Ball MR, Windl W, Woodward PM. Cs₂AgBiX₆ (X = Br, Cl): New Visible Light Absorbing, Lead-Free Halide Perovskite Semiconductors. *Chem Mater.* 2016;28(5):1348-1354. doi:10.1021/acs.chemmater.5b04231
 35. Igbari F, Wang R, Wang ZK, et al. Composition stoichiometry of Cs₂AgBiBr₆ films for highly efficient lead-free perovskite solar cells. *Nano Lett.* 2019;19(3):2066-2073.
 36. Volonakis G, Haghighirad AA, Milot RL, et al. Cs₂InAgCl₆: a new lead-free halide double perovskite with direct band gap. *J Phys Chem Lett.* 2017;8(4):772-778.
 37. Dar SA, Want B. DFT study of structural, mechanical, and opto-electronic properties of scandium-based halide double perovskite Cs₂ScInBr₆ for optoelectronic applications. *Micro and Nanostructures.* 2022;170:207370.
 38. Erum N, Ahmad J, Iqbal MA, Ramzan M. DFT insights of mechanical, optoelectronic and thermoelectric properties for Cs₂ScTiX₆ (X = Cl, Br, I) double perovskites. *Opt Quantum Electron.* 2023;55(4):1-15. doi:10.1007/s11082-022-04538-2
 39. Ashiq MGB, Albalawi H. Study of electronic, mechanical, thermoelectric and optical

- properties of K_2ScAuZ_6 ($Z= Br, I$) for energy harvesting. *Eur Phys J Plus*. 2023;138(6):1-12.
40. Blaha P, Schwarz K, Madsen GKH, Kvasnicka D, Luitz J, others. wien2k. *An Augment Pl wave+ local orbitals Progr Calc Cryst Prop*. 2001;60:1-302.
 41. Perdew JP, Burke K, Ernzerhof M. Generalized gradient approximation made simple. *Phys Rev Lett*. 1996;77(18):3865.
 42. Wimmer E, Krakauer H, Weinert M, Freeman AJ. Full-potential self-consistent linearized-augmented-plane-wave method for calculating the electronic structure of molecules and surfaces: O₂ molecule. *Phys Rev B*. 1981;24(2):864.
 43. Jamal M, Bilal M, Ahmad I, Jalali-Asadabadi S. IRelast package. *J Alloys Compd*. 2018;735:569-579.
 44. Tran F, Blaha P. Accurate band gaps of semiconductors and insulators with a semilocal exchange-correlation potential. *Phys Rev Lett*. 2009;102(22):226401.
 45. Madsen GKH, Carrete J, Verstraete MJ. BoltzTraP2, a program for interpolating band structures and calculating semi-classical transport coefficients. *Comput Phys Commun*. 2018;231:140-145. doi:<https://doi.org/10.1016/j.cpc.2018.05.010>
 46. Goldschmidt VM. Die gesetze der krystallochemie. *Naturwissenschaften*. 1926;14(21):477-485.
 47. Shannon RD. Revised effective ionic radii and systematic studies of interatomic distances in halides and chalcogenides. *Acta Crystallogr Sect A Cryst physics, diffraction, Theor Gen Crystallogr*. 1976;32(5):751-767.
 48. Mir SA, Gupta DC. Analysis of cage structured halide double perovskites Cs_2NaMCl_6 ($M= Ti, V$) by spin polarized calculations. *J Alloys Compd*. 2021;854:156000.
 49. Du X, He D, Mei H, Zhong Y, Cheng N. Insights on electronic structures, elastic features and optical properties of mixed-valence double perovskites $Cs_2Au_2X_6$ ($X= F, Cl, Br, I$). *Phys Lett A*. 2020;384(8):126169.
 50. Ghotra JS, Hursthouse MB, Welch AJ, Soc JC, Trans D. *Inorganic Chemistry, Vol. 17, No. 8, 1978* 2319. 1978;17(8):2319-2320.
 51. Roy M, Ghorui S, Alam A, Aslam M, others. Facile strategy to synthesize cesium gold-based bromide perovskites: an integrated experimental and theoretical approach to study temperature-dependent structural and optical properties. *J Mater Chem C*. 2022;10(11):4224-4235.
 52. Wang S, Hirai S, Shapiro MC, et al. Pressure-induced symmetry breaking in tetragonal $CsAuI_3$. *Phys Rev B - Condens Matter Mater Phys*. 2013;87(5):1-6. doi:[10.1103/PhysRevB.87.054104](https://doi.org/10.1103/PhysRevB.87.054104)
 53. Jain A, Ong SP, Hautier G, et al. Commentary: The materials project: A materials genome approach to accelerating materials innovation. *APL Mater*. 2013;1(1). doi:[10.1063/1.4812323](https://doi.org/10.1063/1.4812323)

54. Bolef DI, Menes M. Measurement of elastic constants of RbBr, RbI, CsBr, and CsI by an ultrasonic cw resonance technique. *J Appl Phys.* 1960;31(6):1010-1017. doi:10.1063/1.1735736
55. Kirklin S, Saal JE, Meredig B, et al. The Open Quantum Materials Database (OQMD): Assessing the accuracy of DFT formation energies. *npj Comput Mater.* 2015;1(October). doi:10.1038/npjcompumats.2015.10
56. Meyer G, Corbett JD. Reduced ternary halides of scandium: RbScX₃ (X= chlorine, bromine) and CsScX₃ (X= chlorine, bromine, iodine). *Inorg Chem.* 1981;20(8):2627-2631.
57. Katsura T, Tange Y. A simple derivation of the Birch--Murnaghan equations of state (EOSs) and comparison with EOSs derived from other definitions of finite strain. *Minerals.* 2019;9(12):745.
58. Markov M, Hu X, Liu HC, et al. Semi-metals as potential thermoelectric materials. *Sci Rep.* 2018;8(1):9876.
59. Tran F, Blaha P, Schwarz K. Band gap calculations with Becke-Johnson exchange potential. *J Phys Condens Matter.* 2007;19(19). doi:10.1088/0953-8984/19/19/196208
60. Nakajima T, Sawada K. Discovery of Pb-free perovskite solar cells via high-throughput simulation on the K computer. *J Phys Chem Lett.* 2017;8(19):4826-4831.
61. Saha T, Babu MMH, Arifuzzaman M, Podder J. Thermodynamic and dynamic stability in a new potential Cs₂AgAsCl₆ perovskite: insight from DFT study. *Phys Chem Chem Phys.* 2022;24(43):26609-26621.
62. Zhang X, Shen JX, Wang W, de Walle CG. First-principles analysis of radiative recombination in lead-halide perovskites. *ACS Energy Lett.* 2018;3(10):2329-2334.
63. Wu B, Zhou Y, Xing G, et al. Long minority-carrier diffusion length and low surface-recombination velocity in inorganic lead-free CsSnI₃ perovskite crystal for solar cells. *Adv Funct Mater.* 2017;27(7):1604818.
64. Gao W, Ran C, Xi J, et al. High-quality Cs₂AgBiBr₆ double perovskite film for lead-free inverted planar heterojunction solar cells with 2.2% efficiency. *ChemPhysChem.* 2018;19(14):1696-1700.
65. Shadabroo MS, Abdizadeh H, Golobostanfard MR. Elpasolite structures based on A₂AgBiX₆ (A: MA, Cs, X: I, Br): Application in double perovskite solar cells. *Mater Sci Semicond Process.* 2021;125:105639.
66. Wang M, Zeng P, Bai S, et al. High-quality sequential-vapor-deposited Cs₂AgBiBr₆ thin films for lead-free perovskite solar cells. *Sol Rrl.* 2018;2(12):1800217.
67. Das S, Debbarma M, Chattopadhyaya S. Calculations of physical properties of Ba₂GdSbO₆ (BGSO) double perovskite for thermoelectric and solar cell applications. *Phys B Condens Matter.* 2023;664:414979.
68. Sa R, Wei Y, Zha W, Liu D. A first-principle study of the structural, mechanical,

- electronic and optical properties of vacancy-ordered double perovskite Cs_2TeX_6 (X= Cl, Br, I). *Chem Phys Lett.* 2020;754:137538.
69. Wuttig M, Schön CF, Schumacher M, et al. Halide perovskites: advanced photovoltaic materials empowered by a unique bonding mechanism. *Adv Funct Mater.* 2022;32(2):2110166.
 70. Fox M. Optical properties of solids. Published online 2002.
 71. Kojima A, Teshima K, Shirai Y, Miyasaka T. Organometal halide perovskites as visible-light sensitizers for photovoltaic cells. *J Am Chem Soc.* 2009;131(17):6050-6051.
 72. Grimes RD, Cowley ER. A model dielectric function for semiconductors. *Can J Phys.* 1975;53(23):2549-2554.
 73. Hu DY, Zhao XH, Tang TY, et al. First-principles study on the structural, elastic, electronic and optical properties of lead-free double perovskites $\text{Cs}_2\text{CuBiX}_6$ (X= Br, Cl). *Mater Today Commun.* 2021;29:102842.
 74. Hu DY, Zhao XH, Tang TY, Li L, Tang YL. Insights on structural, elastic, electronic and optical properties of double-perovskite halides $\text{Rb}_2\text{CuBiX}_6$ (X= Br, Cl). *J Phys Chem Solids.* 2022;167:110791.
 75. Hu DY, Zhao XH, Tang TY, et al. Revealing structural, elastic, electronic and optical properties of potential perovskites K_2CuBiX_6 (X= Br, Cl) based on first-principles. *J Solid State Chem.* 2022;310:123046.
 76. Liu Y, Huang Y, Yang Z, et al. Hexagonal Lead-Free $\text{Cs}_2\text{AgBiI}_6$ Perovskite Nanocrystals: A Promising Material for Solar Cell Application. *ACS Appl Energy Mater.* Published online 2023.
 77. Houari M, Bouadjemi B, Abbad A, Lantri T, Haid S. Lead-Free Semiconductors with High Absorption : Insight into the Optical Properties of $\text{K}_2\text{GeSnBr}_6$ and K_2GeSnI_6 Halide Double Perovskites. 2020;112(6):364-369. doi:10.1134/S0021364020180010
 78. Mahmood Q, Hassan M, Ahmad SHA, Shahid A, Laref A. Journal of Physics and Chemistry of Solids Study of optoelectronic and thermoelectric properties of BaSiO_3 perovskite under moderate pressure for energy renewable devices applications. *J Phys Chem Solids.* 2018;120(February):87-95. doi:10.1016/j.jpccs.2018.04.024
 79. Dhar N, Bandyopadhyay A, Jana D. Tuning electronic, magnetic and optical properties of germanene nanosheet with site dependent adatoms arsenic and gallium: A first principles study. *Curr Appl Phys.* 2017;17(4):573-583.
 80. Li C, Lu X, Ding W, Feng L, Gao Y, Guo Z. Formability of ABX_3 (x= f, cl, br, i) halide perovskites. *Acta Crystallogr Sect B Struct Sci.* 2008;64(6):702-707.
 81. Hegazy HH, Mustafa GM, Nawaz A, Noor NA, Dahshan A, Boukhris I. Tuning of direct bandgap of $\text{Rb}_2\text{ScTiX}_6$ (X = Cl, Br, I) double perovskites through halide ion substitution for solar cell devices. *J Mater Res Technol.* 2022;19:1271-1281. doi:10.1016/j.jmrt.2022.05.082

82. Chen CW, Hsiao SY, Chen CY, Kang HW, Huang ZY, Lin HW. Optical properties of organometal halide perovskite thin films and general device structure design rules for perovskite single and tandem solar cells. *J Mater Chem A*. 2015;3(17):9152-9159.
83. Harris S. *An Introduction to the Theory of the Boltzmann Equation*. Courier Corporation; 2004.
84. Das S, Debarma M, Ghosh D, et al. First-principles calculations to investigate structural, mechanical, electronic, magnetic and thermoelectric properties of Ba_2CaMO_6 (M= Re, Os) cubic double perovskites. *Phys B Condens Matter*. 2022;626:413554.
85. Sajjad M, Mahmood Q, Singh N, Larsson JA. Ultralow lattice thermal conductivity in double perovskite Cs_2PtI_6 : a promising thermoelectric material. *ACS Appl Energy Mater*. 2020;3(11):11293-11299.
86. Reshak AH, Khan SA, Auluck S. Thermoelectric properties of a single graphene sheet and its derivatives. *J Mater Chem C*. 2014;2(13):2346-2352.
87. Kumar A, Bano S, Govind B, Bhardwaj A, Bhatt K, Misra DK. A review on fundamentals, design and optimization to high ZT of thermoelectric materials for application to thermoelectric technology. *J Electron Mater*. 2021;50:6037-6059.
88. Mahmood Q, Hassan M, Flemban TH, et al. Optoelectronic and thermoelectric properties of double perovskite Rb_2PtX_6 (X = Cl, Br) for energy harvesting: First-principles investigations. *J Phys Chem Solids*. 2021;148:109665. doi:<https://doi.org/10.1016/j.jpics.2020.109665>
89. Ali MA, Dar SA, AlObaid AA, et al. Appealing perspectives of structural, electronic, mechanical, and thermoelectric properties of $\text{Tl}_2(\text{Se,Te})\text{Cl}_6$ vacancy-ordered double perovskites. *J Phys Chem Solids*. 2021;159:110258.
90. Liu H, Shi X, Xu F, et al. Copper ion liquid-like thermoelectrics. *Nat Mater*. 2012;11(5):422-425.
91. Albalawi H, Mustafa GM, Saba S, et al. Study of optical and thermoelectric properties of double perovskites Cs_2KTlX_6 (X = Cl, Br, I) for solar cell and energy harvesting. *Mater Today Commun*. 2022;32(July):104083. doi:10.1016/j.mtcomm.2022.104083
92. Iqbal S, Mustafa GM, Asghar M, et al. Tuning the optoelectronic and thermoelectric characteristics of narrow bandgap $\text{Rb}_2\text{AlInX}_6$ (X= Cl, Br, I) double perovskites: A DFT study. *Mater Sci Semicond Process*. 2022;143:106551. doi:<https://doi.org/10.1016/j.mssp.2022.106551>
93. Guechi N, Bouhemadou A, Bin-Omran S, Bourzami A, Louail L. Elastic, Optoelectronic and Thermoelectric Properties of the Lead-Free Halide Semiconductors $\text{Cs}_2\text{AgBiX}_6$ (X = Cl, Br): Ab Initio Investigation. *J Electron Mater*. 2018;47(2):1533-1545. doi:10.1007/s11664-017-5962-2
94. Ehrler B, Alarcón-Lladó E, Tabernig SW, Veeken T, Garnett EC, Polman A. Photovoltaics reaching for the Shockley--Queisser limit. Published online 2020.

